A TOMOGRAPHIC IMAGE OF THE FAULT ZONE ON THE NORTH ANATOLIAN FAULT

By

Tuğçe AFACAN ERGÜN

B.S. Geophysical Engineering, İstanbul Technical University, 2002

Submitted to

Boğaziçi University

Kandilli Observatory and Earthquake Research Institute

in partial fulfillment of

the requirements for the degree of

Master of Science

in Geophysics

Boğaziçi University

June 2006

ACKNOWLEDGEMENTS

I dedicate this work to those who have been with me on this thesis, helping me, supporting me, encouraging me. Throughout my studies at university and the development of this thesis, I benefited greatly from the guidance and encouragement of my advisor Assoc. Prof. Hayrullah Karabulut. I would like to express my special thanks to him for suggesting the topic, supplying many valuable insights and giving freedom to conduct my research in a way that I enjoyed it. His scientific knowledge and professional excellence were enough motivation for me and still is.

I express my special thanks to Esen Arpat. Sharing his knowledge on the geology of the study area and his life experience has been a pleasure for me. I also thank to the members of my Committee, Prof. Dr. Mustafa Aktar, and Assoc. Prof. Serdar Özalaybey for their valuable comments and suggestions. I would like to thank the members of TÜBITAK-Marmara Research Center, Earth and Marine Sciences Research Institute for the collection and providing the seismic data. The seismic experiment would not be performed without the contribution of LGIT. I thank Dr. Michel Dietrich and Dr. Michel Bouchon for their continuing interest.

The outcome documented here has benefited from such an enthusiastic exchange of scientific views of Doğan Aksarı. A long-term friend deserves many thanks for being with me through the vicissitudes in my life. I feel extremely proud and lucky to have such a close and permanent friend who takes care of me all the time.

I thank all the faculty members and staff of the Boğaziçi University, Department of Geophysics. Special thanks to Gülten Polat and Seda Yelkenci for being my friend.

I would like to acknowledge the support of my parents who taught me the value of education and encouraged me through all my life. Heartfelt thanks to my husband for his concern in realizing this goal, for his love and patience during the sleepless nights.

Tuğçe AFACAN ERGÜN

June 2006

ABSTRACT

During the fall of 2003, seismic data were collected in the eastern Marmara Region on the North Anatolian Fault Zone near İzmit rupture zone by a controlled source experiment. The fault was clearly exposed on the surface and the thickness of the sediments in the basin is expected to be greater than several hundred meters. The data were acquired along a 1.2 km long north-south profile with a total of 50 recorders equipped with 4.5 Hz geophones. 3-component geophones were used near the fault zone to detect trapped waves. The shot spacing was 5 m and receiver spacing was varying from 10m to 20m. More than 180 shots were fired using a vibroseis. Data were recorded continuously with 100Hz sampling rate.

This study is a step towards a determination of a shallow P wave velocity structure on the NAFZ near İzmit rupture. We applied regularized inversion technique to the first arrival travel times. More than 6500 picks from 129 shot-gathers were used in the analysis. A shallow P wave velocity image (<200m) from travel time tomography was obtained in the İzmit basin. The results indicate a fault zone of approximately 100 m thick. A velocity contrast was detected between the fault zone and surrounding blocks. The P wave velocity on the southern block varies between a range 1.4 – 1.7 km/s and 1.7 – 2.0 km/s on the northern block the velocity decreases to 1.4 km/s within the fault zone. 3-component recordings and fan shots indicates the presence of the fault zone consistent with the tomographic image. Previous seismological studies in the region also show that the thickness of the fault zone is on the order of approximately 100m.

ÖZET

2003 sonbaharında, Marmara bölgesinin doğusunda, İzmit kırığı yakınlarında Kuzey Anadolu Fay Zonu üzerinde kontrollü kaynak deneyi ile sismik veri toplanmıştır. Basendeki sediman tabakalarının kalınlıklarnın, yüzlerce metre olması beklenmekte ve yüzeyde fay izi rahatlıkla izlenmekteydi. Veri; 1.2 km uzunluğunda, kuzey-güney doğrultulu bir profil boyunca, 4.5 Hz jeofonlara bağlanmış toplam 50 adet kayıtçı ile toplanmıştır. Kanal dalgalarını (trapped waves) görüntülemek için, 3 bileşenli jeofonlar fay zonuna yakın yerleştirilmiştir. Atış aralığı 5 m olup kayıtçı aralıkları 10 ile 20 m arasında değişmektedir. Vibroseis kullanılarak, 180den fazla atış yapılmış ve veri sürekli olarak 100Hz örnekleme aralığı ile kaydedilmiştir.

Bu çalışma; İzmit kırığı yakınlarında Kuzey Anadolu Fayı üzerinde sığ P dalgası hız yapısını belirlemeye yöneliktir. İlk varış zamanlarına, regularize edilmiş ters çözüm yöntemi uygulanarak, analizde 129 atış grubu ile 6500 den fazla ilk varış zamanı kullanılmıştır. İzmit baseninde, seyahat zamanı tomografisi kullanılarak sığ P dalgası (<200m) hız imajı elde edilmiştir. Sonuçlar, fay zonu genişliğinin yaklaşık 100m olduğunu göstermektedir. Fay zonu ve çevreleyen bloklar arasında hız farklılıkları saptanmıştır. Güney bloktaki P dalgası hızı 1.4 – 1.7 km/s, kuzey bloktaki P dalgası hızı 1.7 – 2.0 km/s arasında değişirken hız fay zonunda 1.4 km/s'ye düşmektedir. Bölgede daha önce yapılmış sismik çalışmalarda da fay zonu genişliğinin yaklaşık 100 m olduğu görülmüştür.

TABLE OF CONTENTS

LIST OF FIGURES

LIST OF SYMBOLS

Z	: Jacobian Matrix
e	: Error vector
S	: Cumulative Squared error
δ	: Gauss – Newton adjustment vector
I	: Identity matrix
β	: Marquard factor
χ^2	: Normalized data misfit
M	: Model vector
s	: Slowness
λ	: Tradeoff parameter
C_d	: Data covariance matrix

ABBREVIATIONS

NAFZ	: North Anatolian Fault Zone
NAF	: North Anatolian Fault
KOERI	: Kandilli Observatory and Earthquake Research Center
TUBITAK	: The Scientific & Technological Research Council of Turkey
M_w	: Moment Magnitude
GPS	: Global Positioning System
FD	: Finite Difference
EAF	: East Anatolian Fault
MARNET	: Marmara Network
N-S	: North - South
Hz	: Hertz
IRIS	: Incorporated Research Institutions for Seismology
MHz	: Mega Hertz
S/N	: Signal to noise ratio
1-D	: One Dimensional
2-D	: Two Dimensional
3-D	: Three Dimensional
ACH	: Aki-Christoffersson-Huseybe Method
ART	: Algebraic Reconstruction Technique
RMS	: Root Mean Square
SIRT	: Simultaneous Iterative Reconstruction Technique
ESRI	: The Earth Sciences Research Institute

1. INTRODUCTION

Geophysical data have been usually interpreted by the use of forward and inverse modeling techniques. Among these, tomography has become a standard tool to map the parameters related to the earth structure. The word of 'tomo' was derived from the Greek for 'section drawing'. The technique is based on finding the velocity and reflectivity distribution from a multitude of observations by the reconstruction of a field from the knowledge of linear path integrals through the field (Clayton, 1984).

Aki, Christofferson and Huseybe (1974) developed the first 3-D tomographic inversion method called "ACH" for earth modeling and extended the technique to determine earth's upper mantle velocity structure (Aki et al., 1976, 1977; Aki and Lee, 1976). Within the following years, the method was applied to data from 25 arrays all around the world with apertures ranging from 20 to 3000 km. The results of these studies showed significant 3-D velocity anomalies, with significant implications on tectonics.

Hirahara (1977) obtained the upper mantle velocity structure under Japan delineated the subducting high velocity pacific plate. Clayton and Comer (1983) and Nolet (1985) introduced the iterative matrix solvers, allowing a quantum jump in the number of model parameters. Following these developments, the method is renamed as tomography. The discovery of a global seismic image (Dziewonski and Anderson, 1984; Tanimoto and Anderson, 1984; Woodhouse and Dziewonski, 1984) which correlated well with the pattern of geoid helped to enhance the believability of seismic tomographic image. The studies convinced the seismological community to consider the seismic tomography as a reliable tool for imaging the earth structure.

Significant progress on the speed and accuracy of travel time computation has been made in the following years leading to more robust algorithms. Vidale (1988, 1992) proposed Finite Difference solution to the eikonal equation in 2-D and 3-D complex media. The solution of eikonal equation (1988, 1992), the algorithm for calculating first arrival travel times, was later modified to handle large sharp contrast properly (Hole and Zelt, 1994). Zelt and Barton (1988) studied the Faeroe Basin using two different tomography methods for determining 3-D velocity structure from first arrival travel time data and compared backprojection and regularized inversion methods.

Tomography methods simply can be classified into the groups according to the type and distribution of source and receivers, according to the data sets used and according to the inversion methods involved. The most common applications are earthquake tomography and controlled source tomography (Hirahara, 1993). Tomographic methods can also be classified according to the solution of the linear systems. Backprojection technique requires no matrix inversion and can treat a large number of unknown parameters in contrast to the iterative accurate methods as algebraic reconstruction (ART) and simultaneous iterative reconstruction (SIRT) techniques.

The rapid growth in the number of seismometers, combined with increasing computer power, allowed improvement in the type and quality of seismic images of the crust and lithosphere. An example of improved imaging capability is the inversion of the full seismic waveform, rather than solely traveltimes, in controlled source surveys (Hole et al., 2005). Waveform tomography provides higher spatial resolution on the seismic images than any other technique.

Among the oldest and most fundamental problems in seismology is to understand the nature of discontinuities within the fault zones and determining the velocity depth relation accurately. Major crustal faults are often marked by narrow, on the order of (10-100) m, tabular or wedge-shaped low-velocity fault zones. The detailed analysis of fault zones plays an important role in problems related to fault mechanics, rupture dynamics, wave propagation and seismic hazard. Seismic observations near the fault zones show motion amplifications, long period oscillations, head waves, and travel time anomalies. These anomalies can be used to determine internal structure of fault zone layers. Therefore seismic tomography can be used to image fault zone heterogeneities in a great detail.

Throughout the history, İstanbul and Marmara Region have always been one of the most important centers of the world having rich cultural heritage from the ancient civilizations. Unfortunately, a continental transform fault lies beneath these densely populated, industrialized and intensively cultivated areas. Continental transform faults such as the San-Andreas Fault in California, the Alpine Fault in NewZeland, the North Anatolian Fault (NAF) in Turkey and the Dead Sea Fault Systems, involve complex structural and sedimentary regimes. This complexity relates to the history of displacement along these fundamental components of the global plate tectonic framework (Brew, 2001).

North Anatolian Fault has been interpreted as a transform fault originating from the late Miocene collision of the Arabian and Eurasian plates (McKenzie, 1992). 1500 km long fault extends from about Lake Van to Greece and splits into several branches in the Marmara Region. The North Anatolian Fault system, which accommodates most of the westward motion of Turkey, has a narrow and localized character, clearly defined by the predominantly strike slip surface along its entire 1000 km length, which is associated with series of major earthquakes (Ambraseys, 2002). The NAFZ is remarkably similar to the San-Andreas fault of California in its style of displacement, high seismicity, neotectonic history, presence of creep and problems of seismic hazard evaluation (Barış, 1995). On the other hand, significant contrasts between the two faults exist in their space time patterns of seismicity and in their plate tectonic relationships (Allen, 1982; Turcotte, 1982).

Many examples of the tomography along the fault zones have been presented during the last decade. Most of these studies are related to the strike slip faults with clear surface expressions and fault zones. One of the most striking examples of these types of the faults is North Anatolian Fault Zone. Following the August 17 1999 İzmit earthquake the fault zone properties in İzmit and Düzce areas have been investigated. Ben Zion et al. (2002) discussed the subsurface structure of Karadere-Düzce branch of the North Anatolian Fault; by using, a large seismic data set recorded by a local PASSCAL network during the six months following the 1999 İzmit earthquake. They determined the depth of trapping structure using travel time analysis and waveform modeling. A seismic tomography study in Eastern Marmara region was performed by Karabulut et al. (2003).

The primary purpose of this study is to determine a velocity structure on the North Anatolian Fault in Sarımeşe near the İzmit rupture zone via 2-D tomography inversions. Following the general overview, a controlled source experiment, data acquisition and processing, travel time tomography and the results of the analysis were briefly explained and a 2-D image of the fault zone was presented. Conclusions that are drawn from the overall tomographic images interpreted in section 7.

2. GEOLOGY AND TECTONIC SETTINGS

2.1 Tectonics of the North Anatolian Fault Zone

Tectonically, Turkey lies within the Alpine-Himalayan orogenic zone. The area has been divided into four tectonic units on paleotectonic period. These units are Pontides, Anatolids, Tourids and Border folds (Ketin, 1966). According to plate tectonics theory in the vicinity of the Anatolian block, the Eurasian, the African and the Arabian plates border each other. The relative motions of the African, Arabian and the Eurasian plates (Figure 2.1), mainly dominate the present tectonic regime and the seismicity of Turkey. Northward motion of the Arabian plate relative to the Eurasian plate causes lateral escape of the Anatolian block to the west and the northeastern block to the east, resulting in right lateral motion along the NAF which is the boundary between the Eurasian and Anatolian plates and left-lateral motion along the EAF, which is another transform boundary between the Anatolian and the Arabian plates (McKenzie, 1972; Arpat and Şaroğlu, 1972; Dewey and Şengör 1979).

The NAFZ is the northern boundary of the westward moving Anatolian block and connects the compressional regime in eastern Anatolia with the extensional regime in the Aegean sea region (Barka, 1992; McKenzie, 1972; Şengör, 1979). The Anatolian and Northeast Anatolian blocks are escaping sideways due to collision between the Arabian and Eurasian plates which began 65 million years ago and is still continuing (Barka, 1992). The fault zone is about 1500 km long extending from the Karlıova triple junction in Eastern Turkey to Greece (Barka, 1992; Barka and Kadinsky-Cade, 1988). Recent studies have indicate that the age of the fault is sometime between the late Miocene (about 13Ma) and early middle Pliocene (Şengör et al., 1985, Dewey et al., 1986; Barka and Gülen, 1988, 1989).

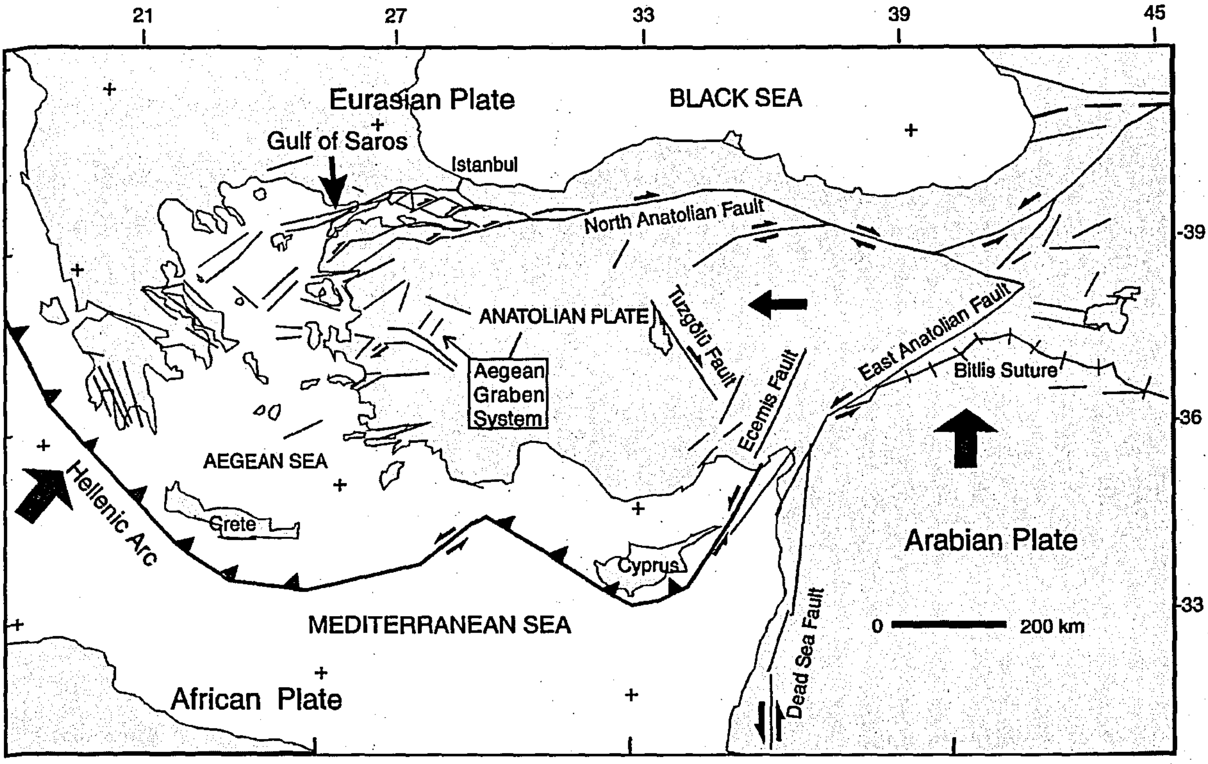

Figure 2.1. Tectonic map of Turkey (Çağatay et al., 1998 modified from Şengör et al., 1985)

The NAFZ shows fishbone characters in middle and eastern parts and has a horse-tail character in the Marmara region and the North Aegean regions (Barka, 1992; Şengör and Barka 1992; Barka and Kandinsky-Cade, 1988). The NAFZ consists mainly of a single strand between the Karlıova to the Mudurnu Valley than splays into three strands in the Marmara and North Aegean regions. The general trend of total displacement along the main part of the NAFZ decreases from 40 ± 5 km in the east to 25 ± 5 km in the west (Barka, 1981, 1985, 1992; Yılmaz, 1985; Koçyiğit, 1989; Barka and Gülen, 1988). The total slip in the Marmara Region is about 30 ± 5 km due to the influence of extension in the Aegean and Western Turkey (Oral et al., 1993; Barka, 1992). The slip rate of the NAFZ is 1 cm/year between Karliova and Erzincan; 0.7 – 0.8 cm/year between Erzincan and Niksar and 0.5-0.6 cm/year between Niksar and Bolu. The slip rate along the western part of the NAFZ for Marmara Region is 2.4 cm/year (Oral et al., 1993). Therefore, the Marmara region is characterized by an active tectonic zone under the influence of the transitional and extensional regimes.

2.2 Local Geology

Marmara Region geologically divided into three parts, namely, Istranca masif, İstanbul zone and Sakarya Zone (Ketin, 1973; Okay, 1986). Between İstanbul zone and Sakarya Zone the Intra-Pontid suture exists which roughly follows the northern strand of the NAF.

The Istranca Massif consists of sandstone, quartzite, shale, limestone and late Permian granitoid deformed and metamorphosed during the late Jurassic. Its contact with the İstanbul zone further east is covered by Eocene sediments.

The İstanbul zone is characterized by a well developed, unmetamorphosed and little deformed continuous Paleozoic sedimentary succession extending from Ordovician to the carboniferous overlain with a major unconformity by latest Permian to lower most Triassic continental red beds (Hoşgören, 1997). The İstanbul zone is very distinctive from the neighboring tectonic units in its stratigraphy., absence of metamorphism and lack of major deformation. The Intra-Pontide suture of Late Triassic-Early Jurassic age separates İstanbul and Sakarya zones. Istanbul zone has a Paleozoic basement (Hoşgören, 1997).

On the other hand, Sakarya zone does not have a Paleozoic basement. The Sakarya zone is characterized by a variably metamorphosed and strongly deformed Triassic basement called the Karakaya complex overlain with a major unconformity by Liassic conglomerates and sandstones which passes up to middle Jurassic lower cretaceous limestones and upper cretaceous flysch (Hoşgören, 1997). Karakaya complex of Triassic age made up of strongly deformed and metamorphosed basic volcanic rocks, limestones and greywackes with limestone olistoliths from the basement to the undeformed post Triassic sediments of Sakarya Zone (Hoşgören, 1997).

The İzmit gulf is an east-west trending active graben, which is dynamically affected by the interaction of the NAFZ and the Marmara Graben systems (Seymen, 1995) is bounded by two horsts: The Kocaeli Peninsula to the north and the Armutlu Peninsula to the south showing completely different geomorphological features and by well-defined fault scarp (Ketin, 1967, Okay 1986).

The Armutlu Peninsula is a narrow linear east-west trending mountain range extending between two fault-controlled gulfs and two lakes formed along the North Anatolian Fault Zone (Yılmaz et al., 1995). The Armutlu Peninsula and the surrounding regions within Northwest Anatolia comprise three geologically different zones: southern, central and northern. The southern zone corresponds to the Sakarya continent and essentially consists of thick Mesozoic sedimentary successions (Figure 2.2) (Yılmaz et al., 1995). The centeral zone mainly consists of the İznik metamorphic assemblage and Geyve metaophiolite. The northern zone is known as the Armutlu metamorphic assemblage and essentially consists of slightly metamorphosed rocks, interpreted as the Rhodope-Pontide basement (Yılmaz et al., 1995).

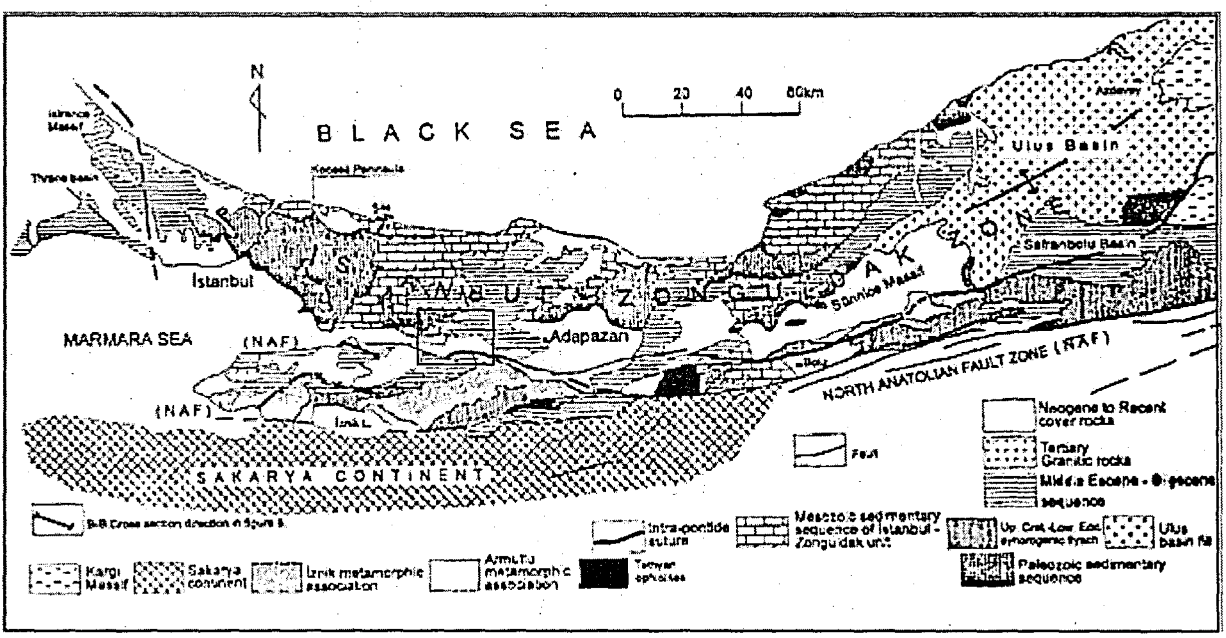

Figure 2.2. Local Geology of Marmara region, red rectangle shows the study area (modified from Yılmaz et al., 1995).

The contact between the equivalent metamorphic and non-metamorphic units of the central and southern zones is sharp everywhere and is defined by a high angle fault which at present corresponds to one of the branches of the NAFZ (Yılmaz et al., 1995).

The Armutlu metamorphic assemblage being part of the Rhodope-Pontide fragment, originally belonged to the Laurasian continent (Şengör and Yılmaz, 1981; Şengör et al., 1985 ; Okay et al., 1994) In contrast the İznik metamorphic assemblage, a part of sakarya continent, belong to the Gondwanaland (Şengör and Yılmaz, 1981 ; Altıner and Koçyiğit, 1992). Therefore the Geyve ophiolite, which is sandwiched between the two collided continental fragments, represent a suture zone and is referred to as the Intra-Pontide suture (Şengör and Y.Yılmaz, 1981).

The Armutlu Peninsula and the surrounding regions represent a collisional mountain belt along which the Rhodope-Pontide fragment collided with and was thrusted over The Sakarya continent. The Geyve metaophiolite that is sandwiched between the two continents therefore represents the ophiolite suture zone known as the Intra-Pontid suture.

The northern part of İzmit Gulf essentially consists of young shallow sediments, beneath these lie a Triassic and Paleozoic sandstone, clay stone and marn. The southern zone corresponds to an olistolitic complex, which is composed of Eosen volcanics (schist, serpantinit and andesit). İzmit Gulf and Sapanca Lake used to be connected to each other. In time, among them is filled up with widespread bog material about 30 – 35 km, and 30 – 40 m thick sediments accumulated over the bog material. Under the experiment area, alluvium deposits and Pliosen sediments of rivers and lakes exist up to 40 meters.

2.3 Seismicity in the Region

The distribution of seismicity within the Alpine–Himalaya system is not homogeneous, the seismic activity being mostly concentrated along the plate boundaries. Boundaries between the Black Sea, Anatolian, Africian and Arabian plates are dominantly responsible for the seismic activity of Turkey. The Marmara region is a tectonically active transition zone between the dextral strike-slip regime of the North Anatolian Fault (NAF) and the extension regime of the Aegean Sea. The North Anatolian Fault Zone has been subjected to repeated moderate and strong earthquakes, as recorded in historical documents and literature (Soysal et al., 1981; Ergin et al., 1967; Okamoto et al., 1970; Sipahioglu, 1982; Ambraseys, 1975; Pınar et al., 1952).

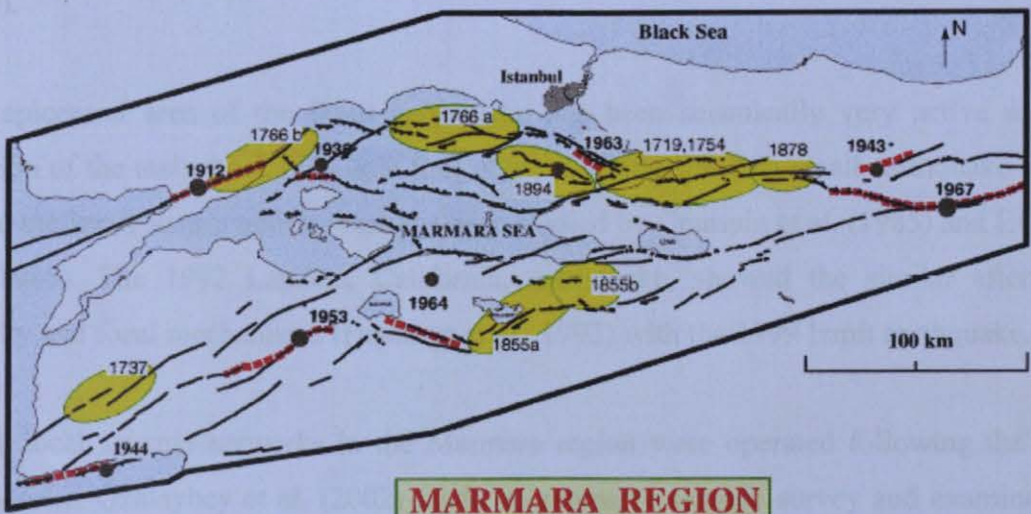

Figure 2.3. Active faulting and historical earthquakes in the Marmara region (modified from Barka, 1997). Black lines: active faults recognized by geology and geophysics. Red lines: surface ruptures of earthquakes of this century. Yellow ellipses: estimated rupture areas of historical earthquakes.

Marmara region is one of the most tectonically active regions on the NAFZ regarding the number of strong earthquakes (Figure 2.3). 17 August 1999 İzmit (Mw=7.4) and 12 November 1999 Düzce(Mw=7.2) earthquakes are the latest and the most destructive ones which caused significant damage and thousands of human loss.

Ambraseys et al. (2002) examined the seismicity of the Marmara Sea in northwest Turkey over the last 2000 year using the historical records. Seismic moment release accounted for the known right-lateral shear velocity across the Marmara region observed by Global Positioning System measurements. The long term seismicity in the Marmara Sea region shows that large earthquakes are less frequent than predicted from the 100-yr long instrumental period (Ambraseys, 2000). Compared with the other parts of the NAF, the Marmara sea region has been one of the rather high seismicity in the twentieth century, releasing a total moment of $6.4*10^{27}$ dyne cm, more than half of which comes from the earthquakes of August 1912 in Ganos and August 1999 in İzmit, with the central Marmara

Basin in between contributing only % 8 of the total seismic moment released (Ambraseys, 2000).

The epicentral area of the İzmit earthquake has been seismically very active and the location of the mainshock falls onto the center of a long-standing small earthquake cluster called the İzmit swarm activity that has been studied by Crampin et al. (1985) and Evans et al. (1985). The 1992 Landers, California, earthquake, showed the similar aftershock activity and focal mechanisms (Haukson et al., 1993) with the 1999 İzmit earthquake.

Many local seismic networks in the Marmara region were operated following the İzmit earthquake. Özalaybey et al. (2002) made an extensive seismic survey and examined the largest earthquake sequence recorded in the history of Turkish earthquakes. They used a local network called ESRI consisting of 54 stations. The aftershock activity spread over an 40 km wide and 170 km long area. Most of the events are located between 5-17 km depth and have strike-slip fault characteristics. There is a lack of seismicity above 4 km (Figure 2.4).

Karabulut et al., (2002) performed a seismic study along the coastlines and islands of the İzmit Bay-Çınarcık basin to clarify the seismic activity that took place after the earthquake. The aftershock distribution indicates three clusters similar to the other studies. One cluster is linear, extends from İzmit Bay to Hersek Peninsula, and defines the fault plane of the main rupture called Central cluster. The second one is Armutlu cluster and the third one is Tuzla cluster. The focal mechanism solutions indicate strike-slip faulting along the main branch of the İzmit rupture and normal faulting within the two swarms (Karabulut et al., 2002). In the light of these conclusions, they show that slip partioning in the region was a plausible mechanism to explain these observations.

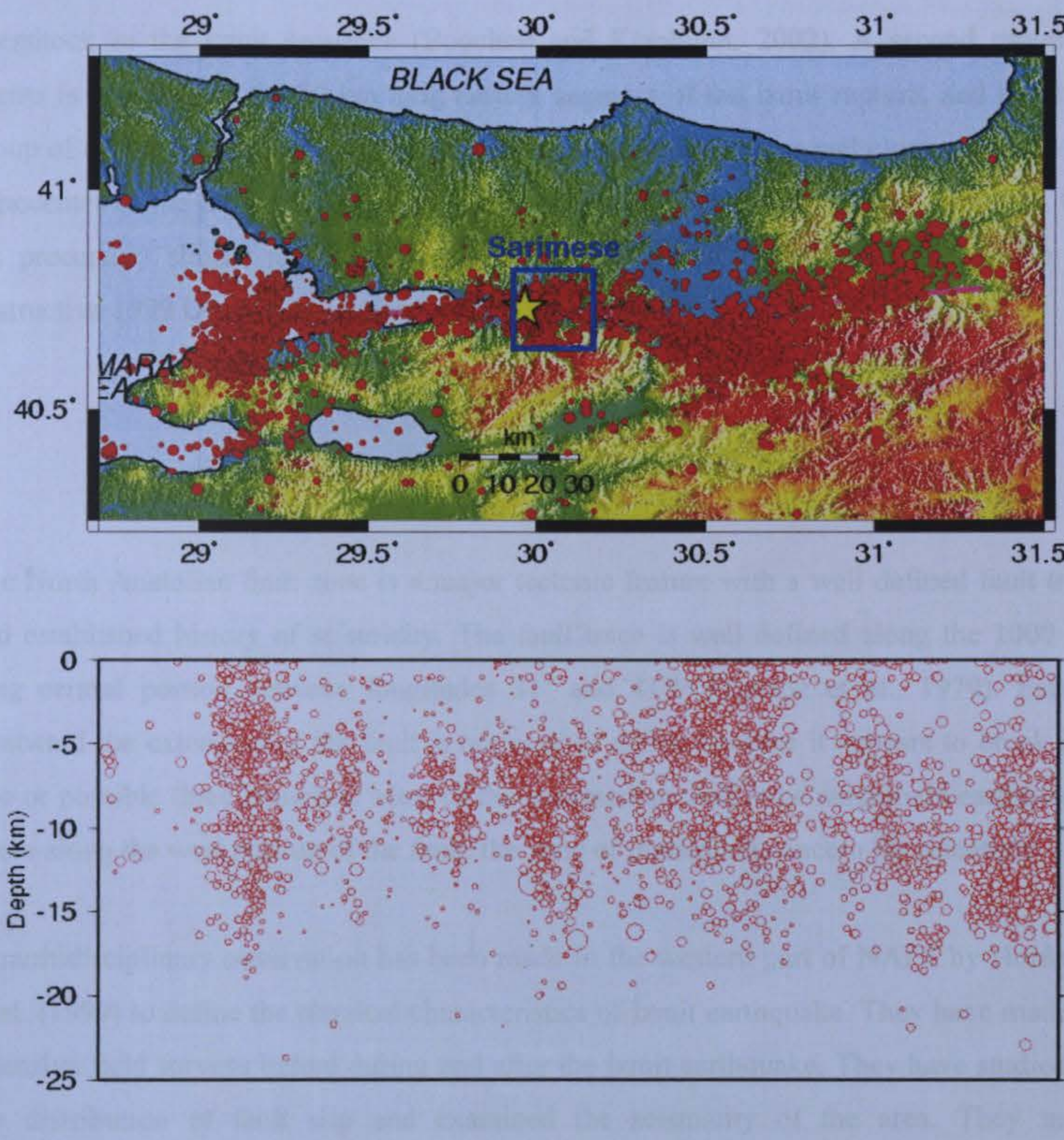

Figure 2.4. Distribution of seismicity and the depth cross section of the İzmit earthquake from 17 August to 20 October 1999 (Tubitak Catalogue (Özalaybey et al., 2002)).

Another noteworthy study on the seismic activity near the eastern termination of the İzmit rupture in the hours preceding the 12 November 1999 Düzce earthquake has been done by Bouchon and Karabulut (2002). They used recordings from four stations installed nearby the eastern termination of the İzmit rupture. They analyzed the seismic activity during the 5 hour before the 1999 Düzce earthquake. The records clearly show the presence of three groups of events. One of the groups originates from the middle of the İzmit rupture and consists of aftershocks of the M 5.7 Sapanca Lake earthquake, the second largest aftershock in the İzmit sequence (Bouchon and Karabulut, 2002). A second group of events is spread over the 30 km long eastern segment of the İzmit rupture, and the third group of events occurs beyond the termination of the İzmit rupture and clusters around the hypocenter of the Düzce earthquake (Bouchon and Karabulut, 2002). They found out that six precursory shocks ranging in magnitude from 0.9 to 2.6 occurred just before the destructive 1999 Düzce earthquake.

2.4 Previous Studies on the Fault Zone

The North Anatolian fault zone is a major tectonic feature with a well defined fault trace and established history of seismicity. The fault trace is well defined along the 1000 km long central portion between longitudes 31° and 41°E (Toksöz et al., 1979). Farther westward the extension of the fault is not easy to define because it appears to break into two or possible three branches. Most of the intermediate and large magnitude earthquakes occur along the west portion of the fault, the zone of immediate concern for scientists.

A multidisciplinary observation has been made in the western part of NAFZ by Honkura, et al. (1999) to define the physical characteristics of İzmit earthquake. They have made an intensive field surveys before during and after the İzmit earthquake. They have studied on the distribution of fault slip and examined the seismicity of the area. They made magnetotelluric surveys to obtain the resistivity structure of the area and realized that resistivity is very low below the northern branch to a depth of 10 km whereas no marked feature was found for southern branch (Honkura et al., 1999).

Several segments of the rupture during the 17 August 1999 have been studied for different aspects of the faulting. Ben Zion et al. (2002) discussed the subsurface structure of Karadere Düzce Branch of the North Anatolian Fault by using a large seismic data set recorded by a local PASSCAL network in the six months following the 1999 İzmit earthquake. The traveltime and waveform analysis of the fault zone trapped waves show that the depth of trapping structure was shallow (3-4 km), and they defined some of the fault zone parameters like thicknesses and velocities.

Karabulut et al. (2003) performed a tomographic study in the Eastern Marmara region. They used seismic refraction data and applied tomographic inversion method to the first arrival travel times to obtain a 2D tomographic image of the NAFZ. The profile extends from Şile to Gemlik along 120 km line and cuts NAFZ crossing the well defined seismicity observed during the aftershock studies (Karabulut et al., 2002). A good correlation between the seismicity and low velocity zones on the two branches of NAF was observed (Figure 2.5).

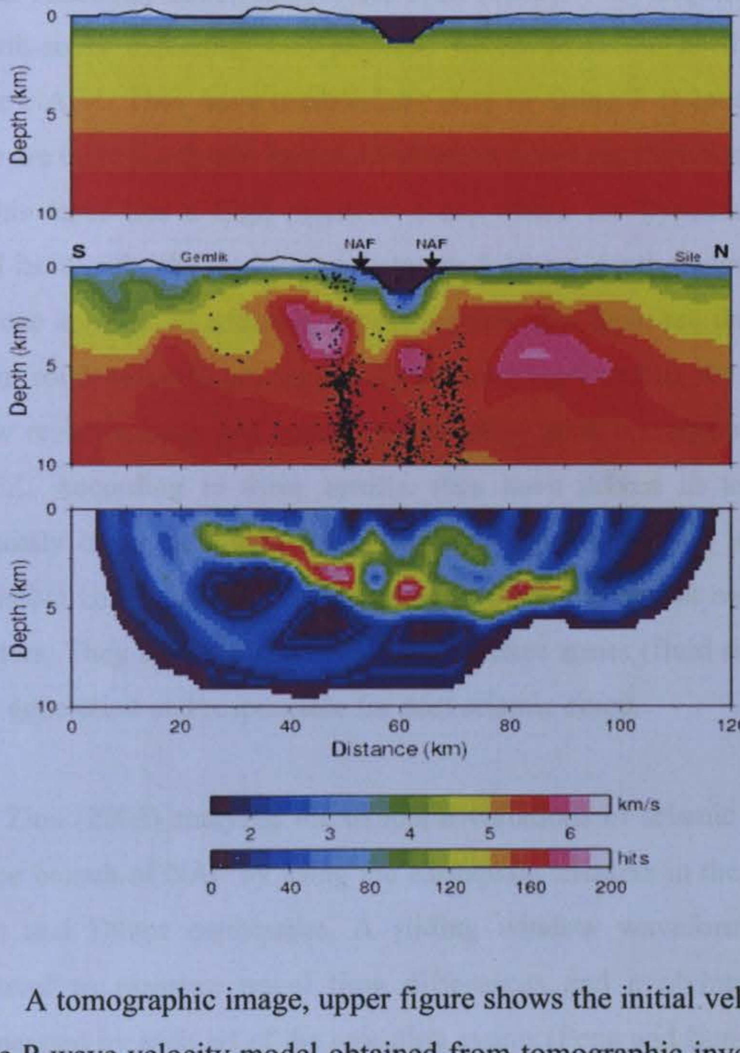

Figure 2.5. A tomographic image, upper figure shows the initial velocity model, middle represents the P-wave velocity model obtained from tomographic inversion and the lower one shows the hitcounts (Karabulut et al., 2003).

Aktar et al. (2004) made an extensive aftershock activity study across the 1999 İzmit earthquake rupture zone. They have made estimations of b-value across the rupture zone. They reached a conclusion that high b-value zones correspond to asperities in the mainschock rupture areas. The results agree with the existence of a deep asperity zone to the east of Sapanca and they added that Yalova-Tuzla section is a pre-existing high fractured filled with fluid and possibly reactivated by coseismic changes in stress.

After the occurence of two large size earthquakes in 1999, the region became very attractive for the scientists. A magnetotelluric survey was carried out in the fault rupture area of the 1999 İzmit earthquake with the purpose of imaging the lower crust upper mantle electrical resistivity structure by Tank et al. (2005). They acquired magnetotelluric data along north-south extending two profiles, which cross the northern and southern branches of the NAFZ. They have modeled the data by using 2-D inversion. The results show that there are three horizontal layers. First one is a low resistive zone between 0-5 km depth under this layer lies a high resistive zone, where the hypocenters of the İzmit earthquake and its aftershocks are located, between 5-15 km depth under this layer another low resistive zone appears. In addition, results indicate that there are three vertical layers. The layers from south to north are high resistive zone representing the southern block of the NAFZ, low resistive zone and again high resistive zone corresponds to the northern block of NAFZ. According to these results, they have driven in to conclusions that earthquakes mostly occur in a high resistivity areas underlain by a low resistive zone. These low resistive zones contain fluids that come from the partial melting occurring at deeper conductors. They also added that the low resistive zones (fluid rich regions) trigger the earthquake generation and responsible for post seismic creep.

Peng and Ben Zion (2005) analyzed the temporal variations of seismic velocity along the Karadere-Düzce branch of NAF by using the earthquake clusters in the afterschock zones of 1999 İzmit and Düzce earthquake. A sliding window waveform cross-correlation technique is used to measure travel time differences and evolving de-correlation in waveforms generated by each set of the repeating events (Peng and Ben-Zion, 2005). They found clear decays in the direct S waves and early S-coda waves, immediately after the Düzce main shock, followed by gradual logarithmic-type recoveries. A gradual increase of seismic velocities is also observed before the 1999 Düzce main shock, probably reflecting post-seismic recovery from the earlier İzmit main shock. A strong correlation between the co-seismic delays and intensities of the strong ground motion generated by the Düzce main shock implies that the radiated seismic waves produce the velocity reductions in the shallow material (Peng and Ben-Zion, 2005).

Overall results from all these studies states that western part of the NAFZ has a really complex, heterogeneous, and fractured structure and provides a challenging environment for new studies.

3. METHODOLOGY

Inversion is a way of obtaining models, which adequately describe a data set (Lines and Treitel 1984). The process is closely related to forward modeling, which uses mathematical relations to synthesize the earth response for a given set of model parameters. Among the several inversion methods, least square inversion is mathematically the most robust technique when the recorded data are inaccurate, insufficient, and inconsistent (Jackson, 1972).

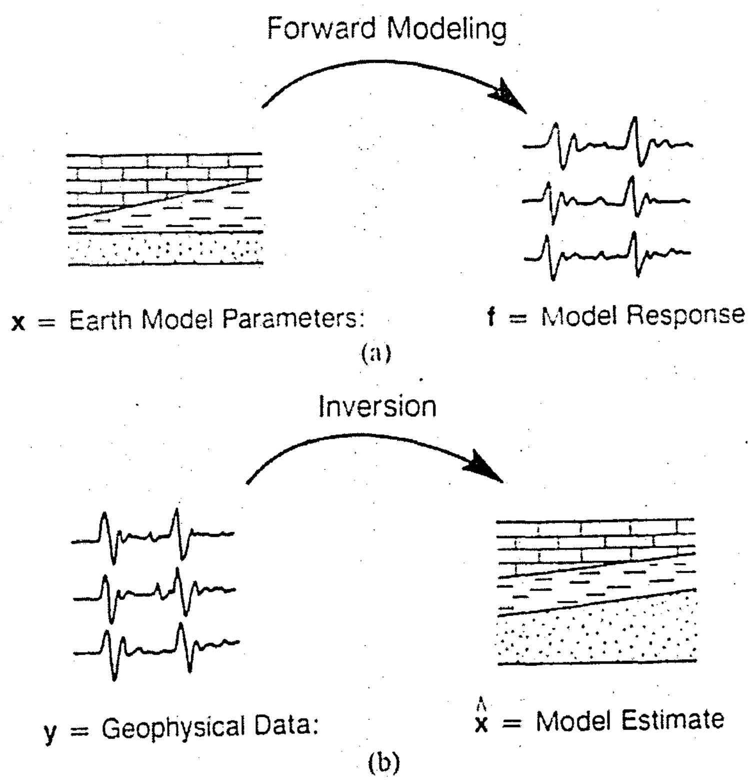

Figure 3.1. An illustration of the objectives of forward modeling and inversion (Lines, 1984).

One of the main advantages of the least square inversion method is its applicability to almost any problem for which a model can be constructed. It is much easier to solve the forward problem that transforms a set of model parameters into a synthetic data set, than to proceed in the opposite direction and solve the inverse problem (Lines and Trietel, 1983).

Having found a method of finding the model response f from the parameters ϕ, Jacobian matrix of partial derivatives must be computed. These derivatives can be determined by formal differentiation if the model response is simple enough. In other cases, partial derivatives must be approximated by finite differences. This can be computationally expensive. Apart from such difficulties, least-square modeling is very versatile and can be adapted to a wide range of geophysical inverse problems (Lines and Trietel, 1983).

3.1 Linear Least Square Inversion

A geophysical inverse problem can be described as the fit of finite set of observations to the response of an idealized earth model. The main idea is to minimize the misfit between the model response and observations. The model response can be either linear or nonlinear function of the model parameters. If the system is nonlinear, it can be linearized by using Taylor series expansion. Let the observations be represented by a vector,

$$y = col\ (y_1, y_2, \ldots, y_n)\ , \tag{3.1}$$

the model response is the vector,

$$f = col\ (f_1, f_2, \ldots, f_n)\ , \tag{3.2}$$

and the model is a function of p parameters,

$$\theta = col\ (\theta_1, \theta_2, \ldots, \theta_p)\ . \tag{3.3}$$

Let θ_j^o be an initial estimate of the parameters and f^0 be the initial model response. If the model response f is a linear function then the perturbation of the model response about θ^o can be represented in matrix notation,

$$f = f^0 + Z\delta\ , \tag{3.4}$$

where Z is the Jacobian matrix which includes partial derivatives of the objective function with respect to model parameters

$$Z_{ij} = \frac{\partial f_i}{\partial \theta_j} , \qquad (3.5)$$

and $\delta = \theta - \theta^0$ is the parameter change vector which represents perturbations. The choice of perturbations in θ will be made so as to minimize the errors. The error vector e is defined as

$$e = g - Z\delta , \qquad (3.6)$$

where, $g = f - f^0$.

In the simplest least square approach, we seek to minimize the cumulative squared error $S = e^T e$ with respect to parameter change vector δ. Minimization of S with respect to δ requires that

$$\frac{\partial S}{\partial \delta} = 0. \qquad (3.7)$$

Carrying out the differentiation with respect to δ gives a linear system of equations called 'normal equations'

$$Z^T Z\delta = Z^T g , \qquad (3.8)$$

whose solution for parameter change vector, δ, is

$$\delta = \left(Z^T Z\right)^{-1} Z^T g . \qquad (3.9)$$

Difficulties arise while finding the inverse of $Z^T Z$ if the matrix $Z^T Z$ is singular. In order to overcome the difficulties Levenberg (1944) and Marquard (1963) introduced an alternate approach to the least squares called 'The Marquard-Levenberg Method'. They replaced the equation (3.9) with

$$\delta = \left(Z^T Z + \beta I\right)^{-1} Z^T g \,, \tag{3.10}$$

where I is identity matrix and β is a constant value, named as 'Marquard factor' or 'damping factor', which may be adjusted to control the iteration step size. If $\beta \Rightarrow \infty$, δ tends to $\theta\, Z^T g$ which is an adjustment in the steepest descent direction. If $\beta \Rightarrow 0$, δ is the Gauss-Newton adjustment vector. The objective of the process is to minimize the sum of the squares of the residuals via steepest descent when the initial estimate of the parameters far from the minimum, and to switch to the rapid convergence of the Newton's method as the minimum is approached.

By using the equation (3.10), the parameter changes are determined from the initial response estimates and an updated set of parameters are obtained to compute the new model response. The iterative search for parameter estimates terminates until the error reaches to smaller values than the specified value.

3.2 Regularized Inversion

Regularization is an approach by which constraints, in addition to the data, are applied to an inverse problem to treat the underdetermined part of the solution (Phillips and Fehler, 1991). Usually the constraints result in the final model satisfying some property in addition to fitting the data, this property is often chosen so that the model has "minimum structure" since we seek models that include only structure that is required to fit the data according to its noise level (Scales et al., 1990). Minimum structure is usually measured in terms of model roughness, e.g., second partial derivative (Parsons et al., 1996).

Regularized inversion minimizes an objective function (model response function) that includes the norms that measure model roughness and data misfit. A tradeoff parameter is also selected to provide the model with the least structure for a given data misfit. It is important to understand that the final model for a nonlinear problem can be a minimum structure if only the starting model is close to the final model.

Minimizing the model roughness for ray-based travel time tomography is important for several reasons; 1) ray methods are valid for smooth media only, 2) travel time constrain only the long wavelength model features since the data represent integrals through the model, 3) linearization assumption of stationary ray paths is more likely to be satisfied for smooth models.

To penalize total model roughness jumping strategy (Shaw and Orcutt, 1985) is used. The objective function minimized at each iteration is,

$$\phi(m) = \delta t^T C_d^{-1} \delta t + \lambda\left[m^T C_h^{-1} m + s_z m^T C_v^{-1} m\right] \tag{3.13}$$

where m is the model vector, δt is the data residual vector, C_d is the data covariance matrix, C_h and C_v are the horizontal and vertical roughening matrices, respectively; λ is the tradeoff parameter, and s_z is the vertical slowness. The system of equations

$$\begin{bmatrix} C_d^{-1/2} Z \\ \lambda C_h \\ s_z \lambda C_v \end{bmatrix} \delta m = \begin{bmatrix} C_d^{-1/2} \delta t \\ -\lambda C_h m_0 \\ -s_z \lambda C_v m_0 \end{bmatrix} \tag{3.14}$$

Where Z is the partial derivative matrix with elements, m_0 is the current model, δm is the model perturbation, and $m = m_0 + \delta m$. The roughening matrices contain the 2-D and 1-D second derivative finite difference operators that measure the model roughness in the horizontal and vertical directions. The normalization by the prior slowness is applied to avoid a bias toward greater levels of model roughness in high velocity regions.

The advantage of regularized inversion is the ability to include prior information, such as solution simplicity, so that it can provide the minimum structure model for a given level of fit to the data (Zelt and Barton, 1998). According to conventional viewpoint, the disadvantages of backprojection are its tendency to produce smeared results and its sensitivity to anisotropic ray coverage. The disadvantages of regularized inversion are its computational and memory requirements and the arbitrariness of the parameter values that determine the tradeoff between data fit and the solution of the prior constraint equations (Zelt and Barton, 1998).

3.3. Seismic Tomography

Tomography is a type of inverse problem. Measurements are first made of some energy that has propagated through a medium. The received character of this energy (amplitude, travel-time) is then used to infer the values such as velocity, density and permittivity of the medium through which it has propagated.

The tomographic problem can be defined as "From projections measured outside of an object find the interior distribution of values inside the object." A projection is the sum of an object's parameters along a given linear energy transit path. A sum or integral of this type is also known as a Radon transform.

The Radon transform is the forward part of the tomographic problem. Then, in the tomographic procedure, we must take these projections and create an image from them. There are two broad categories of techniques used to infer the medium's internal values from the projections. They are "transform" and "series expansion" methods.

- **Transform techniques**

Transform methods start with the motion of an object being described by a continuous function, with a continuous set of projections. Fourier techniques and the filtered backprojection are the two main transform methods.

- **Fourier transform technique**

The Fourier projection theorem states that the 2-D (3-D) Fourier transform of an image or medium can be obtained form the 1-D (2-D) Fourier transforms of the projections. Thus, by measuring the projection of the object and constructing the 2-D (3-D) transform space accordingly, then inverse 2-D (3-D) Fourier transforming, an image of the object may be reconstructed. A major difficulty with this reconstruction is that it requires a complete (all the way around the objects) set of projections.

- **Backprojection method**

Backprojection is an operation which sums projected values (Radon transforms) together. The basic idea is that each point that is traversed by the ray from the source to receiver is given the value of the total projection. The image is constructed by summing the all the values of the points determined for every ray.

This backprojection method can be used to create images, but it is one that leads to blurring of the final reconstructed image. To attain a better image, it is reasonable to attempt a spatial deconvolution. This method is called "filtered backprojection", the notion arising of filtering the backprojection to provide a clearer image. The advantage of backprojection is its minimal computational and memory requirements and therefore the ability to use relatively fine model grids to allow spatial resolution.

Transform methods have been assumed that energy propagates as a ray. However, elastic or acoustic waves have well known properties of divergence and diffraction in accordance with the wave equation. It is nonetheless possible to build wave equation propagation into a tomographic framework. This method is called "diffraction tomography" (DT). Examples of DT inversion methods are "filtered backpropogation algorithms".

- **Series Expansion Methods**

The series expansion methods start by considering the object or area of interest to be comprised of boxes or pixels. Energy is considered to propagate through the various pixels to provide a sum or projection of the pixel values. The pixel values are now related to the sum. These methods provide stable but approximate solutions, and often related to solving large linear equations. Most common one is known as backprojection. In the matrix formulation backprojection corresponds to using the transpose of matrix instead of the inverse. Two other more accurate but iterative methods are known as ART (Algebraic Reconstruction Technique) and SIRT (Simultaneous Iterative Reconstruction Technique). On the other, these techniques require high-capacity computers.

4. DATA ACQUISITION

4.1 Study Area and Experiment Layout

During the fall of 2003, seismic refraction data were collected in the eastern Marmara Region on the North Anatolian Fault Zone near İzmit. The area is located between İzmit Bay and Sapanca Lake (Figure 4.1). The fault, ruptured during 17 August 1999 earthquake, was clearly exposed on the surface where the thickness of the sediments in the basin is expected to be greater than several hundred meters. The traces of the surface rupture could still be recognized on the surface after four years from the earthquake (Figure 4.2). The thickness of the fault zone on the surface appeared to be varying from several meters to several hundred meters.

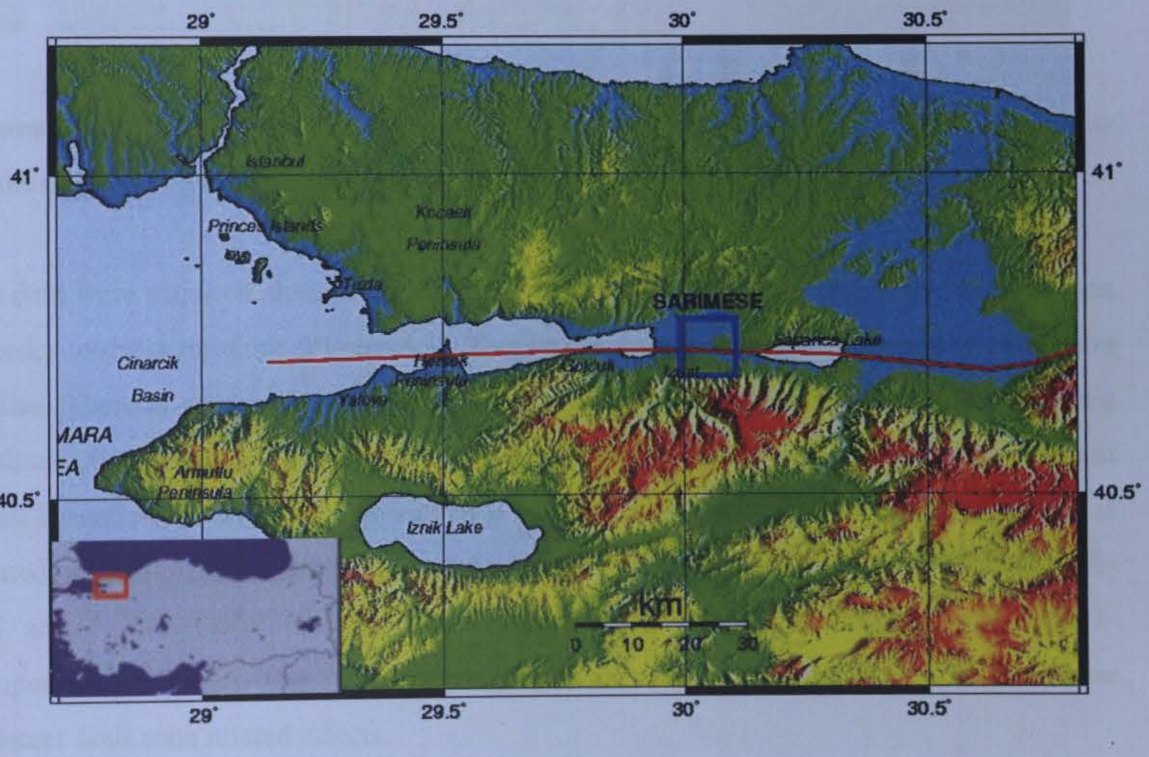

Figure 4.1. Location map of the study area shown by the square box. The red line shows the surface rupture of the 17 August 1999 İzmit (Mw=7.4) earthquake.

Figure 4.2. Surface deformations of the 17 August 1999 İzmit Earthquake near Sarımeşe (Dietrich et al., 2005).

The data were acquired along a 1.2 km long N-S profile which has been attentively chosen in order to cross the fault (Figure 4.3). The survey area is identical for seismic refraction studies. There is mild topography along the profile and the elevation difference between north and south is approximately 19 m increasing from south to north. The profile was cut by an irrigation channel with a width of 6 m. The fault traces observed on the surface is located on the northern continuation of the channel. The line contains a total of 45 Reftek-125 and 5 Reftek-130 recorders equipped with 4.5 Hz vertical component and 3-component geophones. The 3-component geophones were deployed close to the fault zone to detect fault zone related effects.

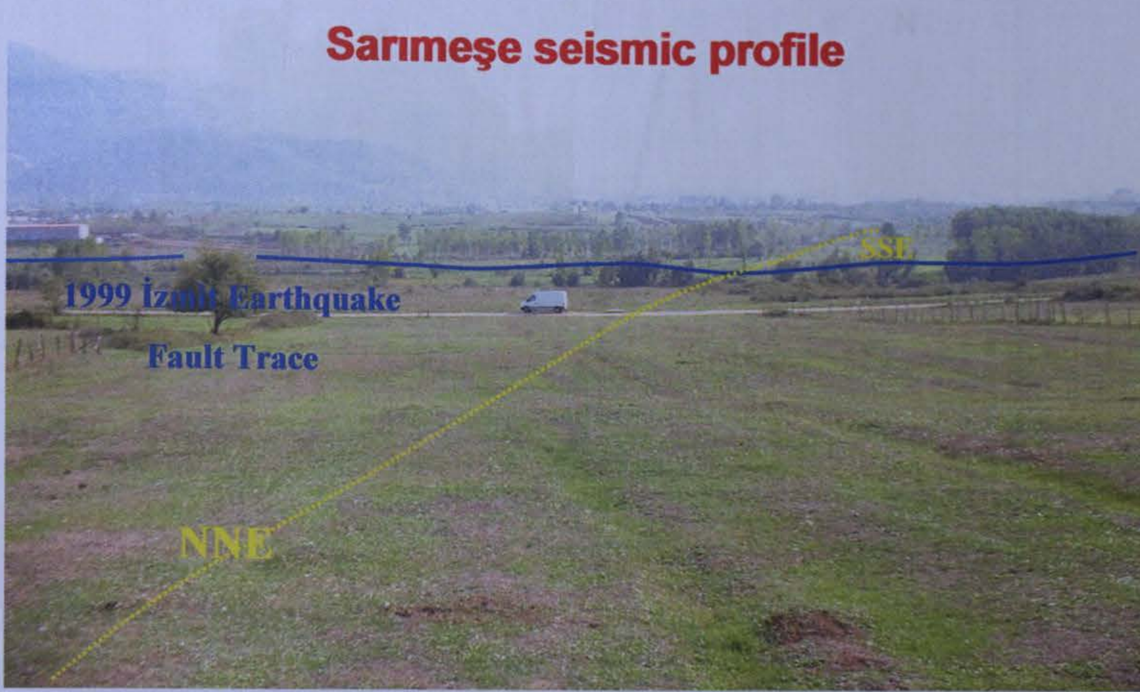

Figure 4.3. Location of the Sarımeşe seismic profile. Yellow dashed line shows the seismic profile, blue line shows the 1999 İzmit Earthquake fault trace (Dietrich et al., 2005).

The shot spacings were 5 m for inline, 200 m for fan shots (on the fault zone) and the receiver spacing was varying from 5m to 20m. More than 180 inline, 10 fan shots were fired using a vibroseis source (Figure 4.4). Due to the vegetation, the geometry of the line was not straight but crocked on the south of the fault zone. The data were recorded continuously with 100 Hz sampling rate.

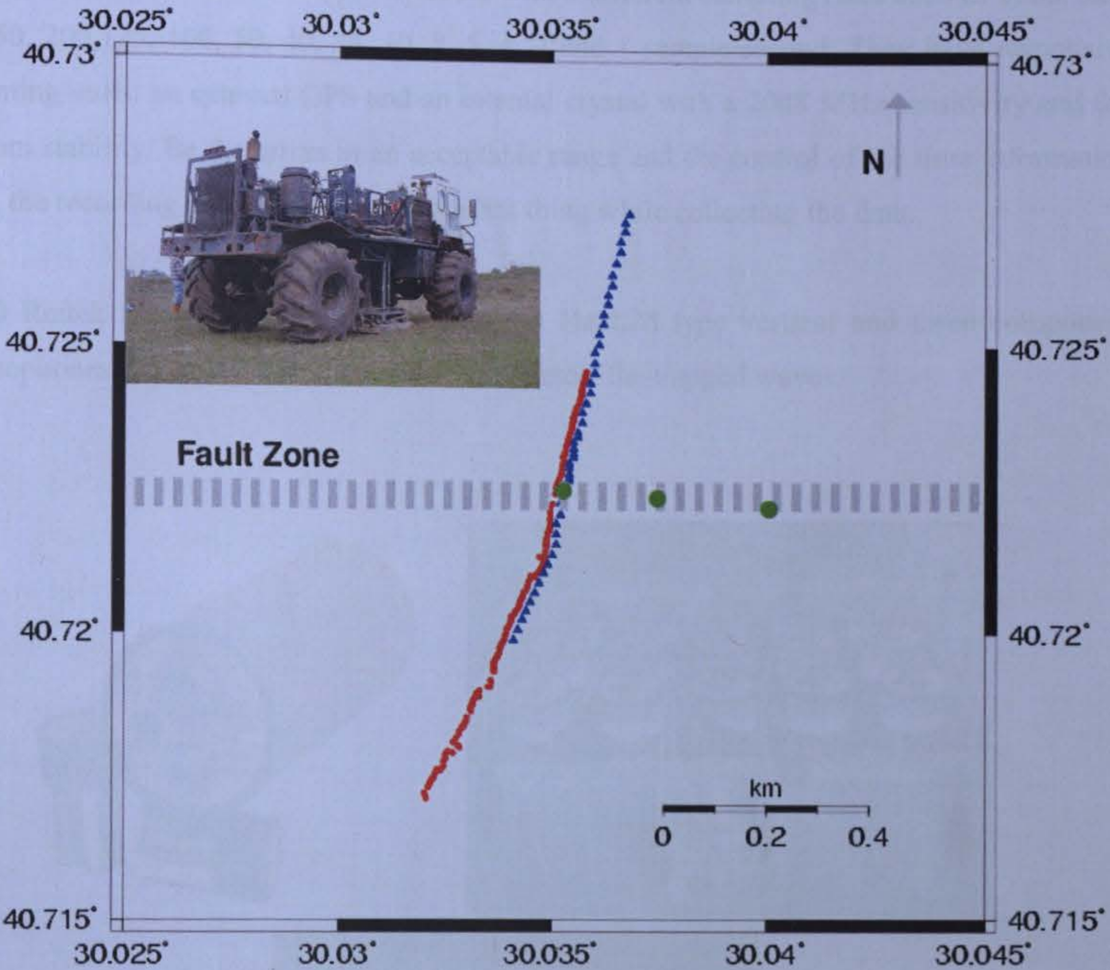

Figure 4.4. The source-receiver geometry of the experiment. Blue triangles indicate the receiver locations and red circles indicate shot locations. Green circles are the fan shots. On the left corner vibroseis unit which was used during Sarımeşe seismic experiment.

4.2 Instrumentation

Specially designed, new generation seismic recording units called Texan Reftek-125's have been used during the 2003 fall experiment. These portable, light in weight and work with low power recording units have been produced by a consortium between Refraction Technology and IRIS (Figure 4.5). They are being used in seismic reflection-refraction surveys, microtremor and aftershock studies since their first production in 1999. Texan's can take continuous records for 72 hours with a different sampling rates such as 1000, 500, 250, 200,125, 100, 50, 40, 25, 10, 8, 5, 4, 2 and 1 sample/second. They have responsive timing units: an external GPS and an internal crystal with a 2048 MHz sensitivity and 0.1 ppm stability. Be the errors in an acceptable range and the control of the time information in the recording units is the most important thing while collecting the data.

50 Reftek-125 recorders equipped with 4.5 Hz L28 type vertical and three component geophones were used near the fault zone to detect the trapped waves.

Figure 4.5. Reftek-125 unit (Top-left), Transcase unit (Top-right), connection of the geophones with Texan (bottom).

5. DATA PROCESSING

5.1 Creating Shot Gathers

We used a geophone close to the vibrator to record sweep signal, which allowed determining origin times more accurately. The distances between the receivers and source points were calculated using a reference point 5m away from the southern end of the profile. The data continuously recorded in REFTEK format were converted into SEG-Y format for each receiver. The continuous SEG-Y data for each receiver were cut into 30-second files from the origin time of each source and converted into SAC format. Then, we formed shot gathers by merging 30-second sac files and sorting as a function of distance. Figure 5.1, an example of an uncorrelated shot gather, shows that the S/N ratio decreases fast at distances grater than 400 m. The trace at 0 m shows the sweep signal recorded next to the vibrator truck. We created a total of 129 shot gathers along 1.2 km long profile.

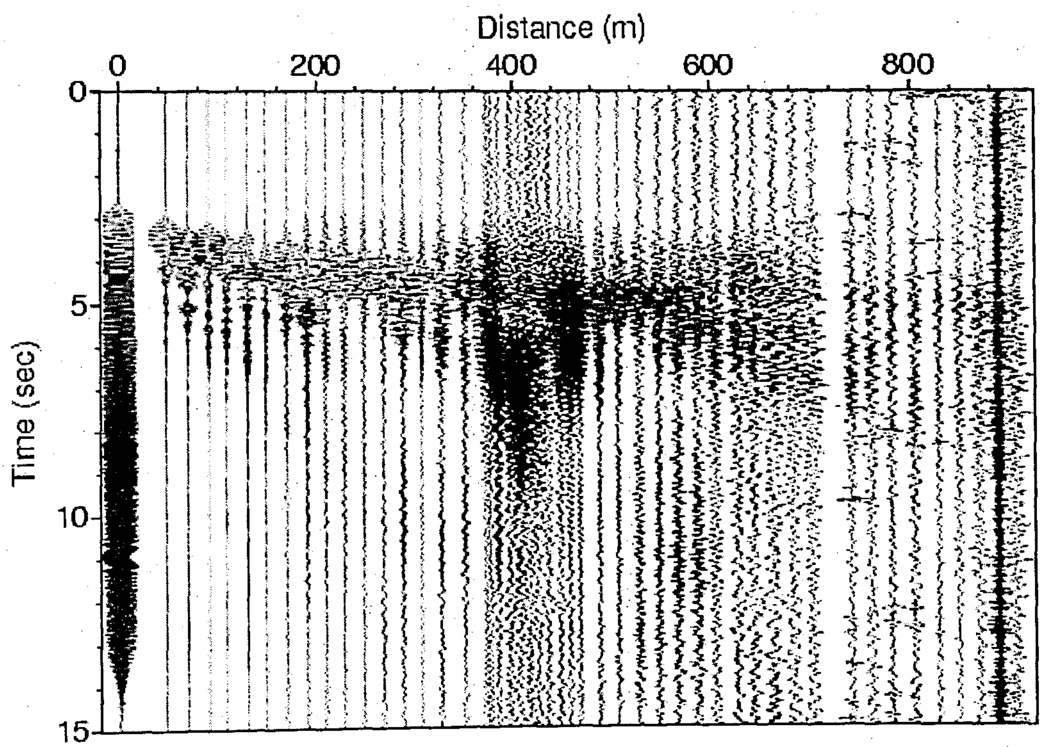

Figure 5.1. The sweep signal and uncorrelated shot gather as a function of distance. The amplitudes were normalized by the maximum of each trace.

5.2 Generating a Sweep Signal

A vibrator is a vehicle-mounted energy source in land surveys that produces a vibratory or swept frequency signal (sweep signal) of relatively long duration (Figure 5.2). Because the signal put into the earth persists a long time, the reflection signals recorded in the field are entirely incoherent to the eye and special processing is necessary to convert the data into usable form.

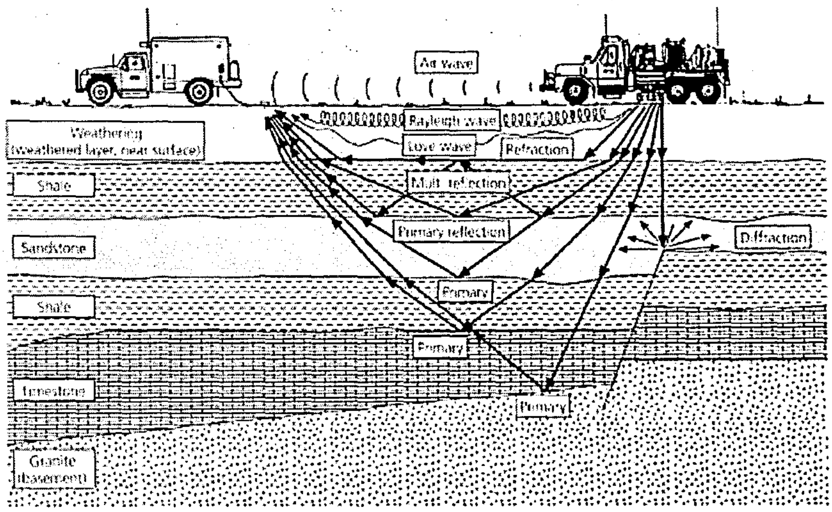

Figure 5.2. Schematic geometry of a Vibroseis survey (Stein, 2003).

The analytic form of the sweep signal can be calculated using

$$w(t) = \cos 2\pi\left(f_1 t + \frac{f_2 - f_1}{2T} t^2 \right) \qquad (5.1)$$

where f_1 and f_2 are initial and final sweep frequencies, respectively, T is time duration of the signal. An example of sweep signal with a time length of T=30 s and a frequency range within 10 Hz – 50 Hz is shown in Figure 5.3.

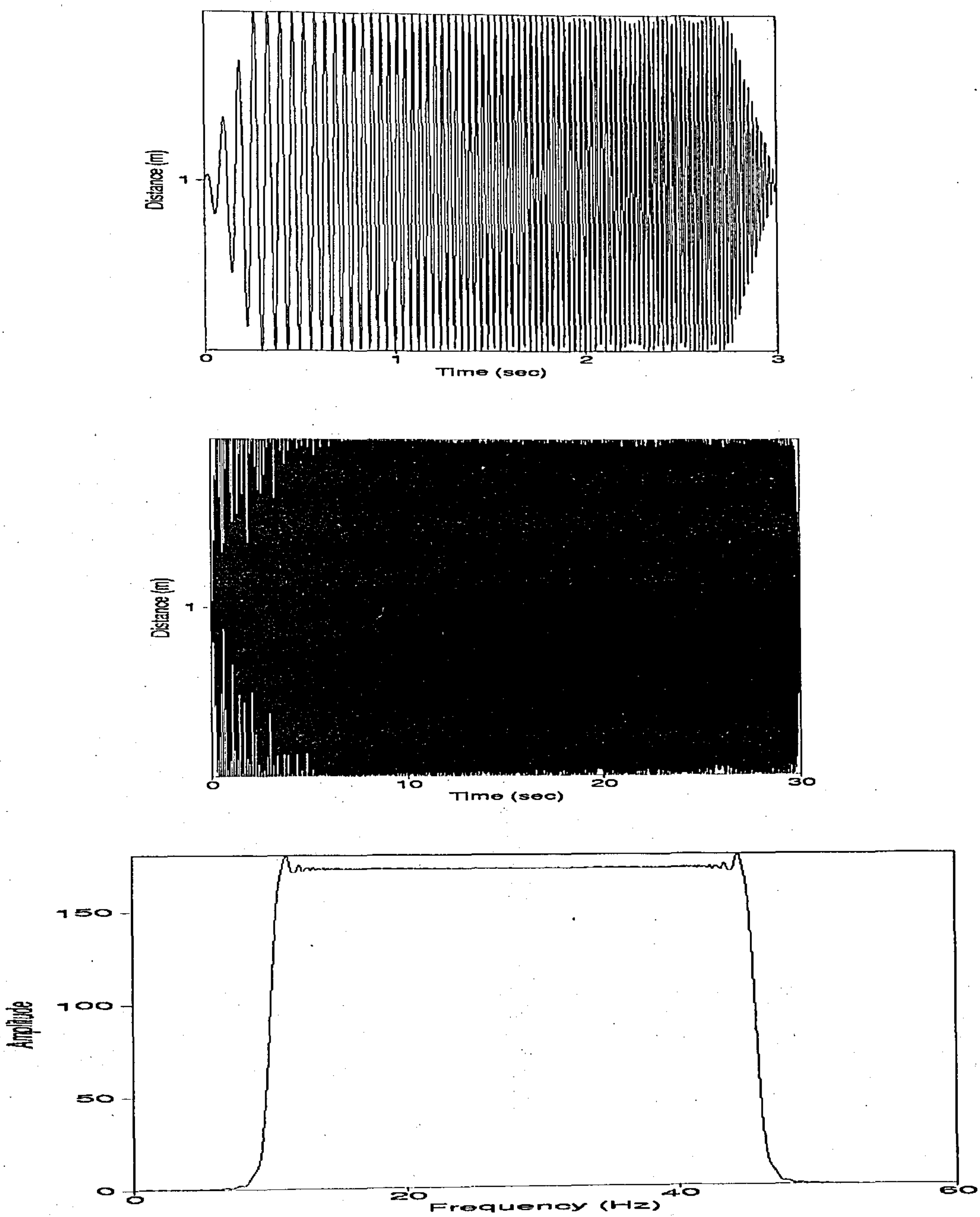

Figure 5.3. Top: Sweep signals for parameters (f1=10 Hz, f2=50 Hz T=3s). Middle: The sweep signal for parameters (f1=10 Hz, f2=50 Hz T=30s). Bottom figure indicates the amplitude spectra of the generated sweep signal.

The sweep signal used during the experiment extends for a period of 15 s over which the frequency varies through a range, within 10-110 Hz.

A reflection record obtained from a vibroseis source consists of superimposed signals from each reflecting surfaces. Each reflection has similar waveforms as the source signal, but the source signal corresponding to each reflector is delayed by the reflection time and scaled by the reflection coefficient of the layer interface. In order to obtain a conventional seismic response similar to the ones obtained using explosive source it is necessary to cross correlate the sweep signal with recorded vibroseis signals. The auto-correlation of a vibrator sweep gives the Klauder wavelet, which is sharply picked at zero lag (Figure 5.4).

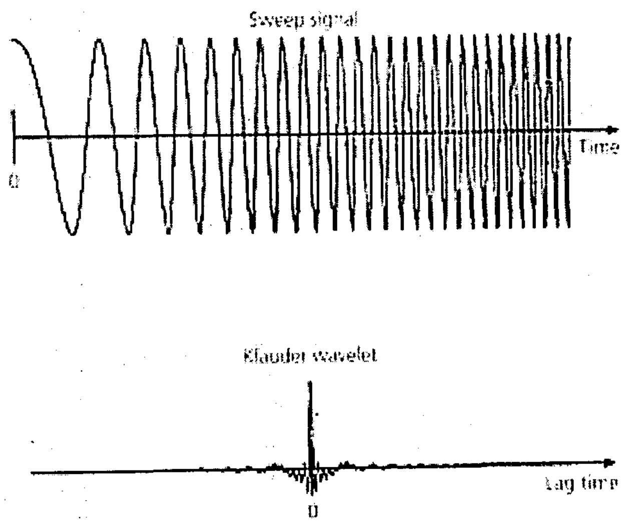

Figure 5.4. The auto-correlation of a sweep signal is an impulsive Klauder wavelet (Stein, 2003).

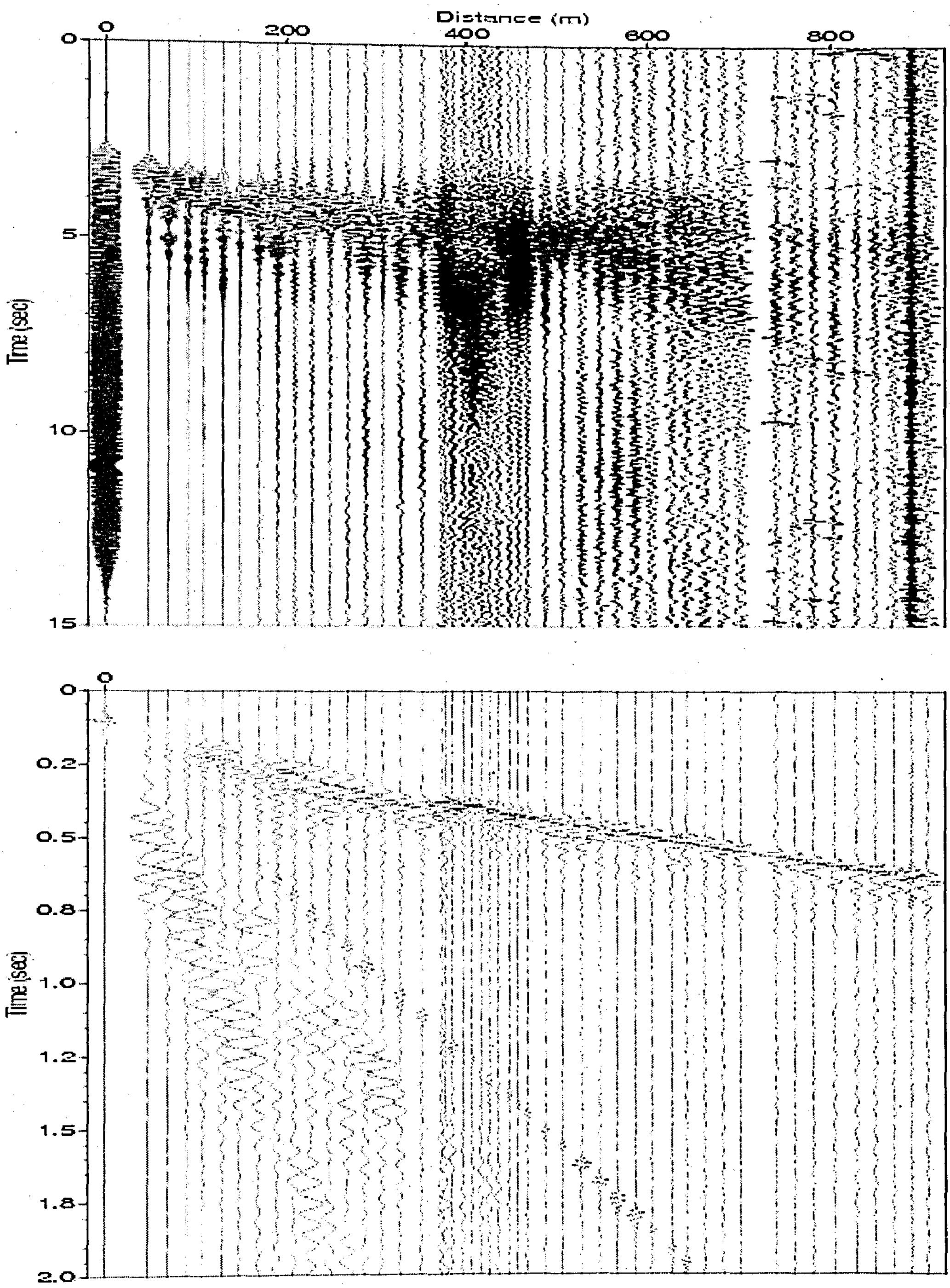

Figure 5.5. Uncorrelated shot gather (top) and correlated shot gather using theoretical vibroseis sweep signal (bottom).

We tested both theoretical and recorded sweep signal to obtain conventional shot gathers. As a result of the analysis we concluded that the theoretical sweep signal provides a better source wavelet. The poor results obtained from the recorded sweep signals might be related to the calibration of the vibrator base plate as well as other components. The poor coupling between base plate and the ground will also give a poor Klauder wavelet. It is expected that the quality of sweep signals will directly determine the resolution.

Theoretically, we expect to see sharp picks at waveforms like in Klauder wavelet but in practice, it is not so simple, because the duration of the sweep is often longer than the difference in travel time between interfaces. The resulting seismogram is a complicated combination of sweep signals with different amplitudes and time delays reflected from different interfaces (Figure 5.6).

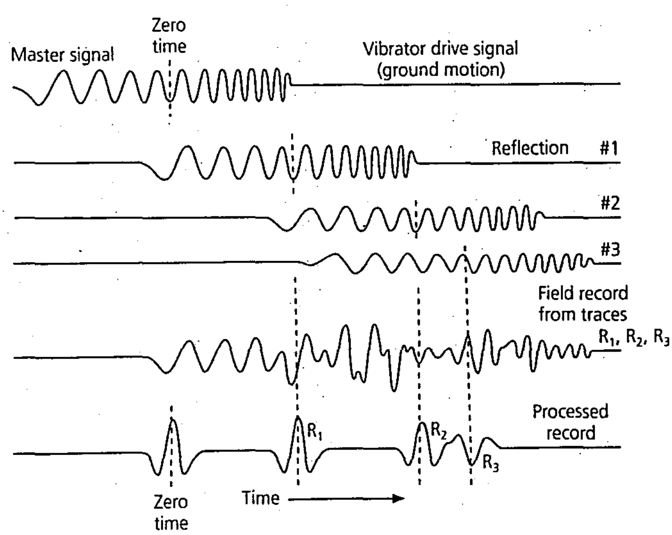

Figure 5.6. Analysis of a vibrator record (Stein, 2003).

5.3 Picking up the Arrival Times

After creating the shot gathers in SEG-Y format, we used an interactive plotting and picking software developed by Zelt (1997) called ZPLOT. The program has been used extensively in refraction analysis and includes features such as plotting, filtering, data editing, calculation of power spectrum. Figure 5.7 shows an example of a shot gather anpicked first arrivals by using ZPLOT. First arrivals were picked for each shot gather and put into an appropriate format for travel time tomography. The uncertainty for each pick was assumed as 10 msec and constant for each shot gather.

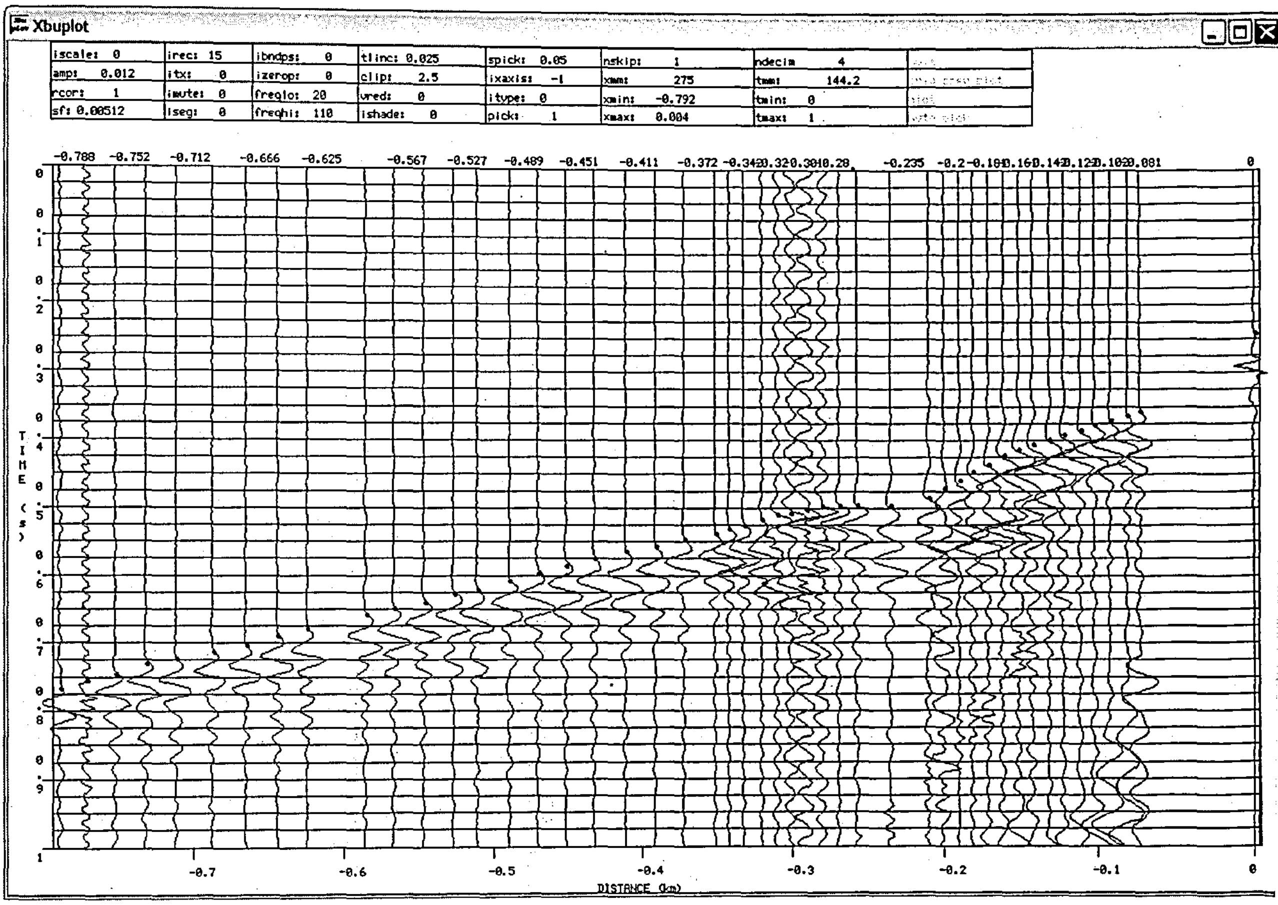

Figure 5.7. An example of a shot gather with the picked first arrivals in ZPLOT window.

6. FIRST ARRIVAL SEISMIC TOMOGRAPHY

6.1 Introduction

The Earth's crust displays a heterogeneous structure on a wide range of spatial scales, including discontinuities, faults, layering, intrusions and partial melt. Imaging this complex structure mainly depends on the density of ray sampling, proportional to the minimum wavelength of the recorded seismic wave energy (Thurber, 1993). First arrival times represent direct, refracted or turning energy. The first arrival travel time tomography provides a valuable tool to obtain a heterogeneous image of the earth both in depth and in distance. The maximum length of the array as well as velocity structure determines the depth of penetration.

The inversion technique used in this study is developed by Zelt (1998). The method, as explained previously, is using a regularized inversion scheme with flattest and smoothest perturbation constraints. The models are parameterized using uniform square grids. The forward grid has much smaller grid spacing than the inverse grid since the accuracy of the computed travel times using Eikonal equation depends on the grid spacing. On the other hand, the inverse grid with the smoothness constraints should be larger to keep the linear system overdetermined. In addition, the smaller grid size for the inverse model is unnecessary since we already impose smoothness in the solution. Sources and receivers may be anywhere in the model.

The regularization is a jumping method in that the constraints are applied to the model perturbation with respect to the initial velocity model. A starting model and iterative approach is used in which new ray paths are calculated for each iteration. First arrival, travel time tomography produces a smooth version of the true velocity model. The inversion is parameterized and the convergence is controlled to produce a minimum structure model.

6.2 Travel Time Distance Curves

We selected 129 shot gathers and picked more than 6500 first arrivals. We ignored approximately one-third of the shot gathers due to the low signal to noise ratio or large uncertainty on the origin times. Figure 6.1 displays the first arrival times of the selected shot gathers along the profile. The coverage in the center of the profile is not uniform due to the lack of shot and receiver points within the irrigation channel. Travel time curves show strong velocity variations along the profile. This is more pronounced at the center of the profile, between 550 and 700m, where the fault scarps on the surface are clearly observable.

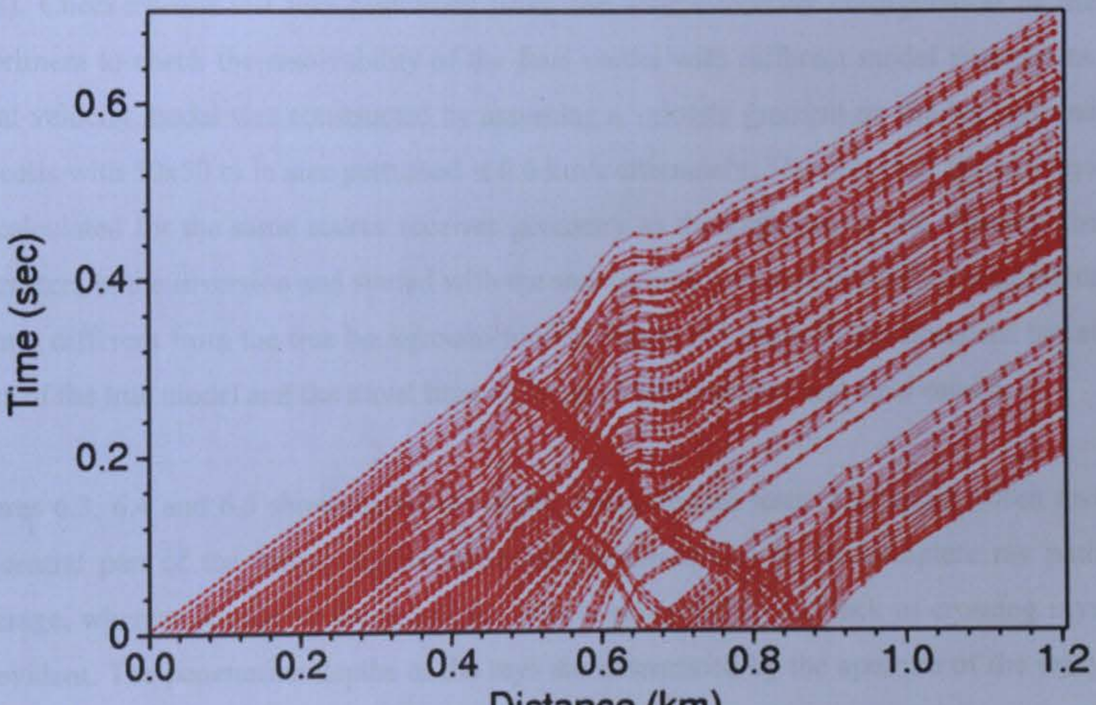

Figure 6.1. The selected travel time curves used to invert 2D velocity structure.

6.3 Checkerboard Test

One of the main difficulties encountered in tomographic studies is the determination of the reliability of the results. Tomographic images reflect not only true velocity heterogeneities but also the effect of data errors, model parameterization and ray path geometry.

The correct assessment of model parameterization in seismic tomography is a difficult task since the resolution of the solution is highly affected by the chosen model parameters. Synthetic tests such as checkerboard test provide information relevant to the model parameterization, damping factor and solution quality (Humpreys and Clayton, 1988; Zelt, 1988). Checkerboard test was performed using the source-receiver configuration of the experiment to check the resolvability of the final model with different model parameters. Initial velocity model was constructed by assuming a velocity gradient on the background and cells with 50x50 m in size perturbed ± 0.6 km/s alternately. The observed travel times are calculated for the same source receiver geometry as the experiment. We changed the parameters in the inversion and started with the same initial model with a velocity gradient slightly different from the true background model. Figure 6.2 displays the observed travel times of the true model and the travel time differences between true and final model.

Figures 6.3, 6.4 and 6.5 show the results of the checkerboard tests. The upper 100m and the central part of the pattern appear quite well retrieved due to the complete ray path coverage, whereas at edge of the model the effects generated by the lack of crossing rays are evident. The penetration depths of the rays are determined by the aperture of the array and the velocity gradient of the medium. The larger velocity gradient causes the rays bend at shallower depths, therefore limits the resolvability at greater depths. The resolution of a tomographic image is determined by ray density, which is related to the source and receiver spacing. However, we expect a smooth image of the true velocity model since travel times delays are related to the velocity structure by the integral along the ray path. We impose smoothness constraints during the inversion knowing that we cannot recover velocity perturbations with wavelengths smaller than average source receiver spacing. The larger values of the smoothness cause decrease in resolution. This can be observed by comparing the result in the Figures 6.3, 6.4 and 6.5 which increasing values of smoothness constraints were used.

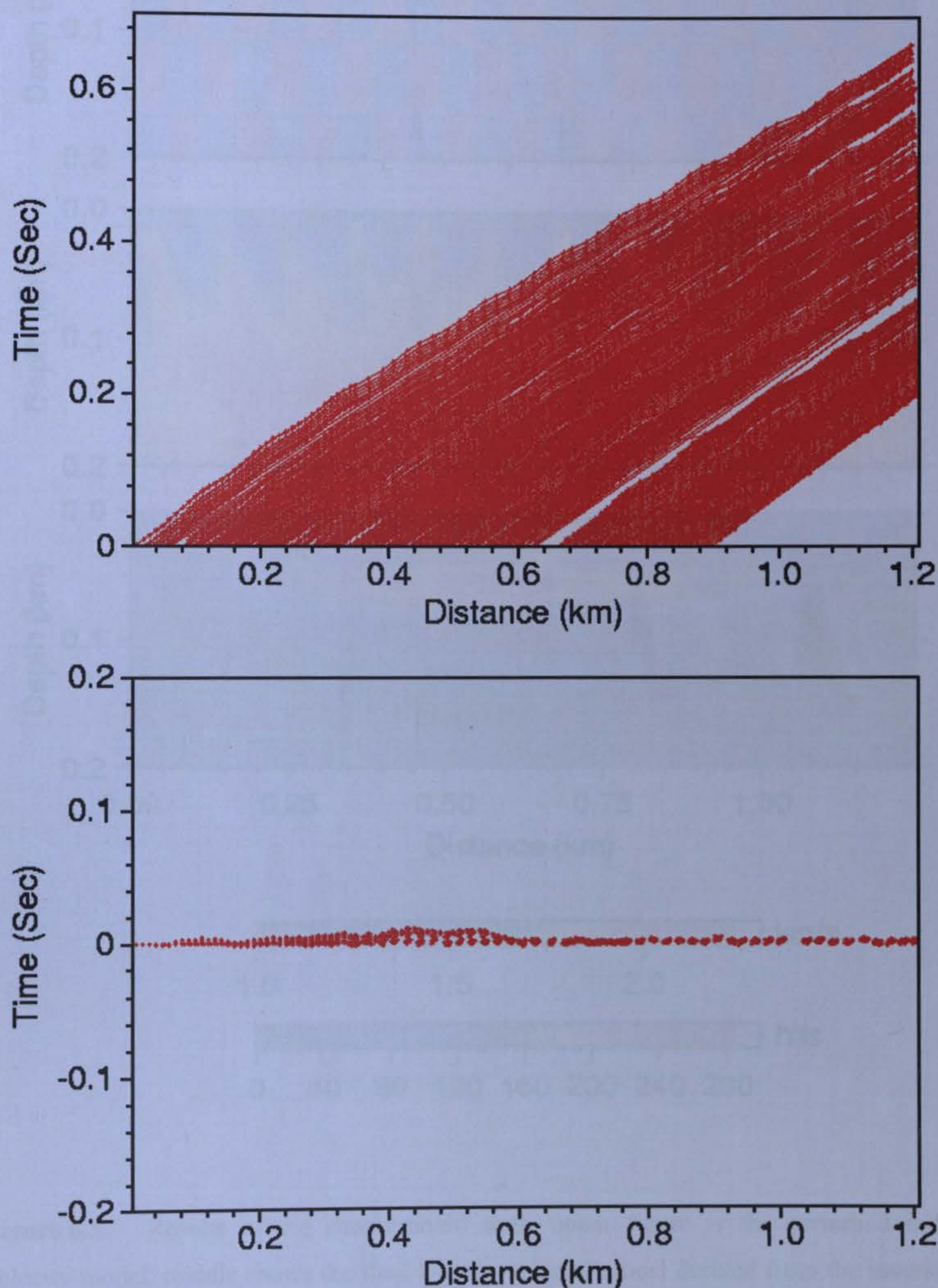

Figure 6.2. Observed travel times for the true model (top) and the travel time differences between true and final model (bottom).

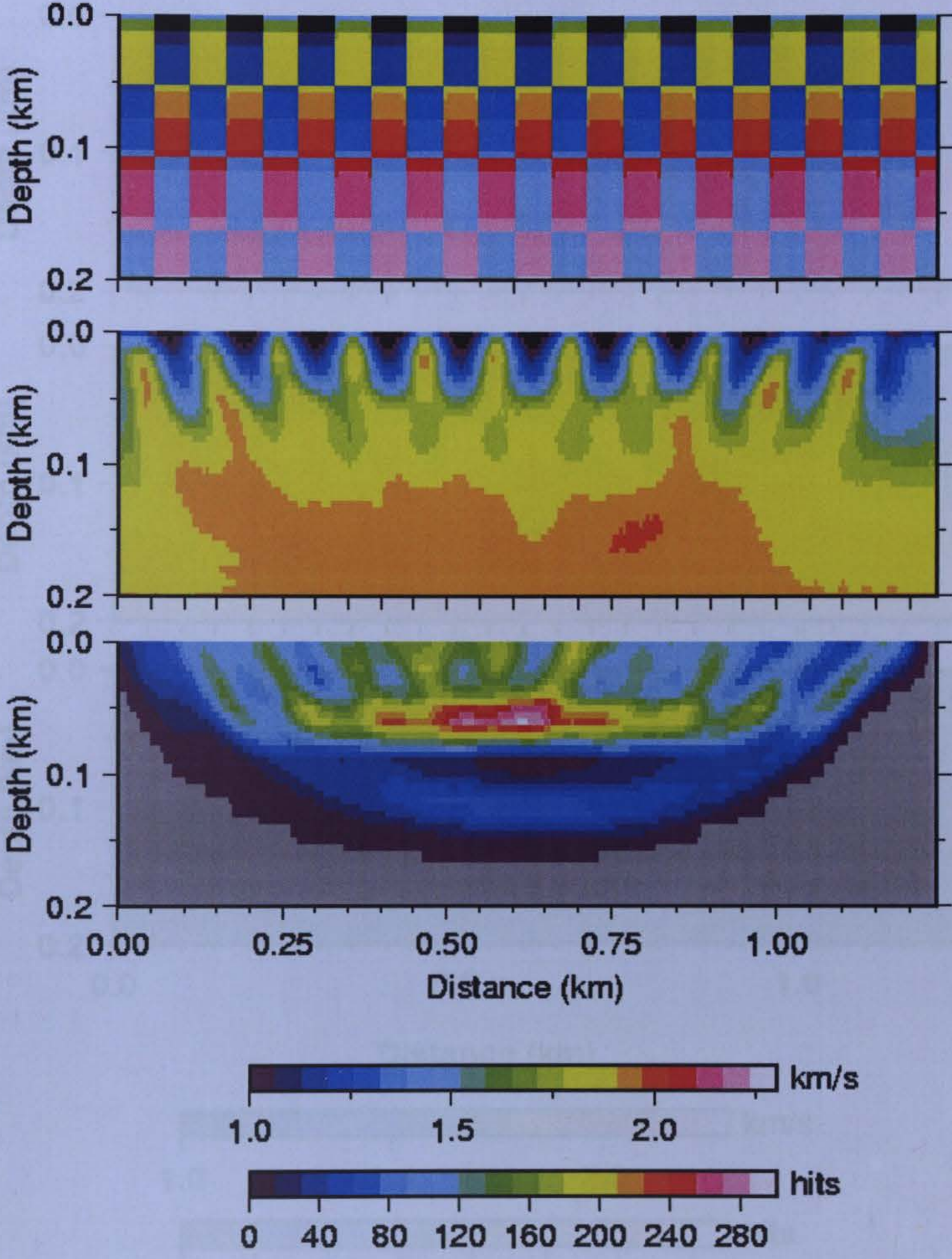

Figure 6.3. Results of the checkerboard tests, upper figure is the perturbed initial velocity model, middle shows the final P-wave velocity model derived from the inversion with smoothness/flatness regularization constraint s_{mwz} = 0.3, lower figure is the ray hitcount.

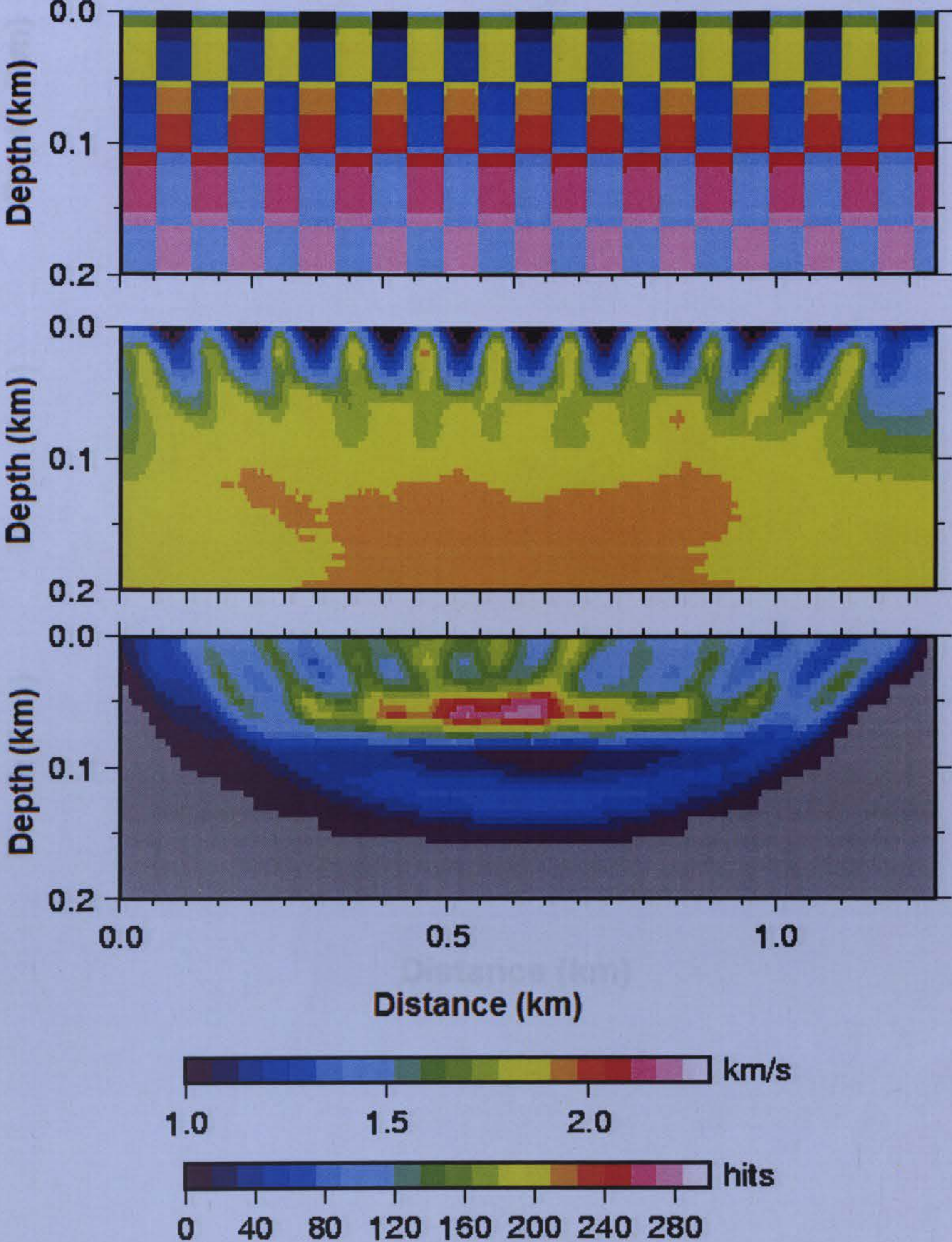

Figure 6.4. Results of the checkerboard tests, upper figure is the perturbed initial velocity model, middle shows the final P-wave velocity model derived from the inversion with smoothness/flatness regularization constraint $s_{mwz} = 0.5$, lower figure is the ray hitcount.

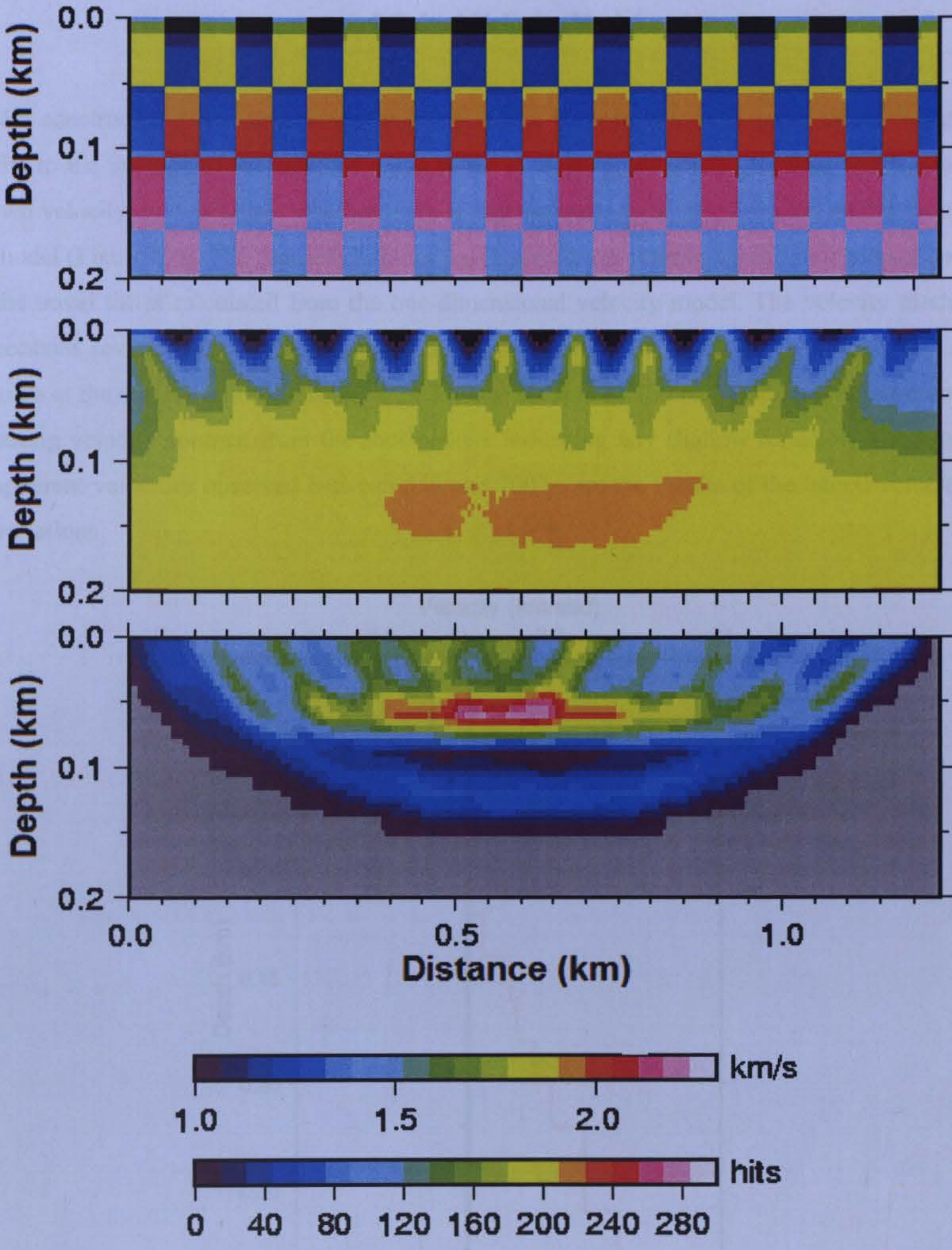

Figure 6.5. Results of the checkerboard tests, upper figure is the perturbed initial velocity model, middle shows the final P-wave velocity model derived from the inversion with smoothness/flatness regularization constraint s_{mwz} = 0.9, lower figure is the ray hitcount.

6.4 Initial Velocity Model

We constructed a one-dimensional velocity model by computing the travel times, which fits to the average of the selected travel times in least-square sense. We also constructed two velocity models to test whether there is any dependency of the inversion on the initial model (Figure 6.6). The Figure 6.7 shows the observed travel times for the shot gathers and the travel times calculated from the one-dimensional velocity model. The velocity model contains several layers of increasing velocity with depth. The velocities are starting at 1.4 km/s at the surface and increasing to 2.2 km/s at a depth of 260 m. We do not observe any strong velocity contrast from the shot gathers indicating any shallow reflector. The high apparent velocities observed between 550 and 700 m are the results of the lateral velocity variations.

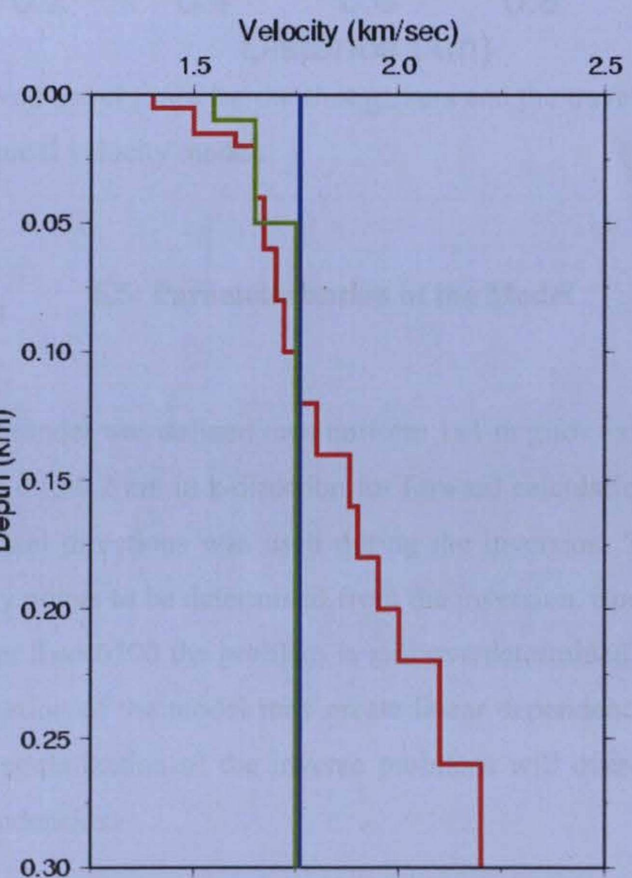

Figure 6.6. Three different velocity models are shown. Red plot indicates the preferred average 1-D velocity model obtained from the traveltime curves, green includes three layers and the blue one represents a constant velocity model.

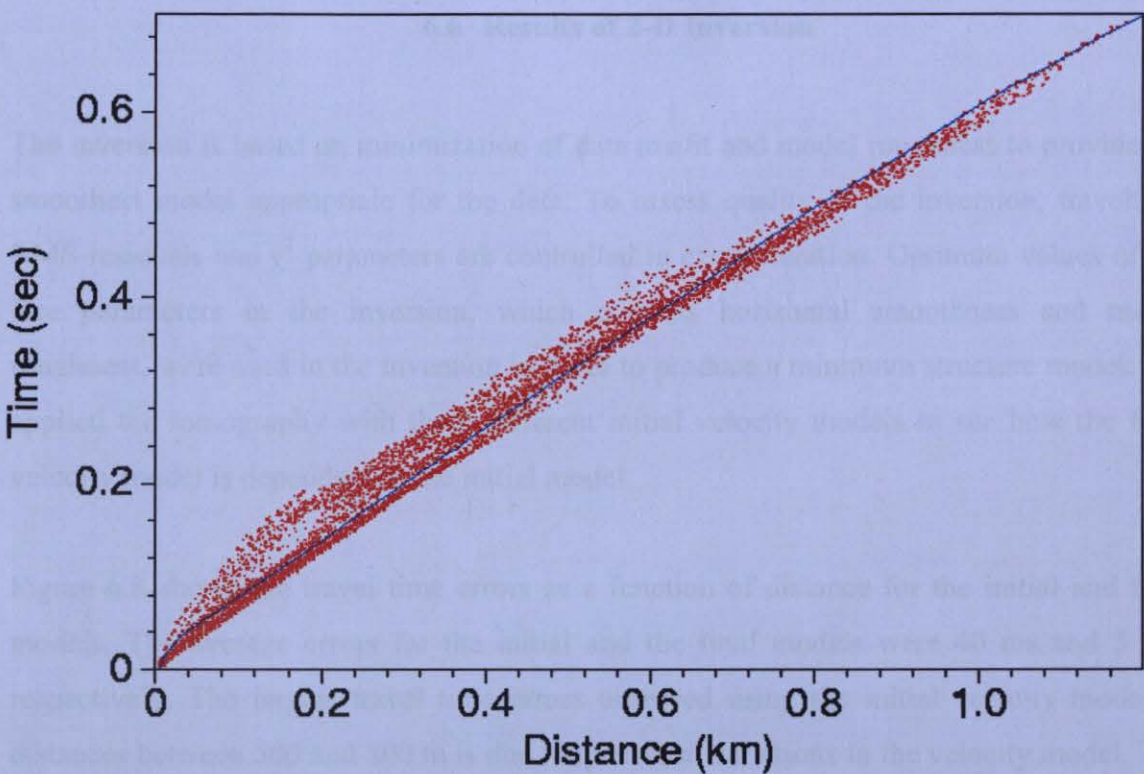

Figure 6.7. Observed travel times for the shot gathers and the travel times calculated from the one-dimensional velocity model.

6.5 Parameterization of the Model

The constant velocity model was defined on a uniform 1x1 m grids extending from 0 to 1.2 km in x-direction and 0 to 0.2 km in z-direction for forward calculations. A grid size of 10 m in lateral and vertical directions was used during the inversion. The parameterization requires 1200 velocity points to be determined from the inversion. Since the number of the observations is greater than 6500 the problem is still overdetermined. However, ray paths covering the same portion of the model may create linear dependencies in the system. In the mean time, the regularization of the inverse problems will overcome the difficulties related to linear dependencies.

We also tried to correct for the topography. This was accomplished by inserting elevation differences into the model. The topography was assumed as a layer with a very low velocity (100 m/s). The sources and receivers were put on the basement of the layer and the velocity of the layer was fixed during the inversion.

6.6 Results of 2-D Inversion

The inversion is based on minimization of data misfit and model roughness to provide the smoothest model appropriate for the data. To assess quality of the inversion, traveltime RMS residuals and χ^2 parameters are controlled in every iteration. Optimum values of the free parameters in the inversion, which controls horizontal smoothness and model roughness, were used in the inversion in order to produce a minimum structure model. We applied the tomography with three different initial velocity models to see how the final velocity model is dependent to the initial model.

Figure 6.8 shows the travel time errors as a function of distance for the initial and final models. The average errors for the initial and the final models were 40 ms and 5 ms, respectively. The largest travel time errors observed using the initial velocity model at distances between 500 and 800 m is due to the lateral variations in the velocity model. The final velocity model reduced the errors, which shows more uniform distribution along the profile.

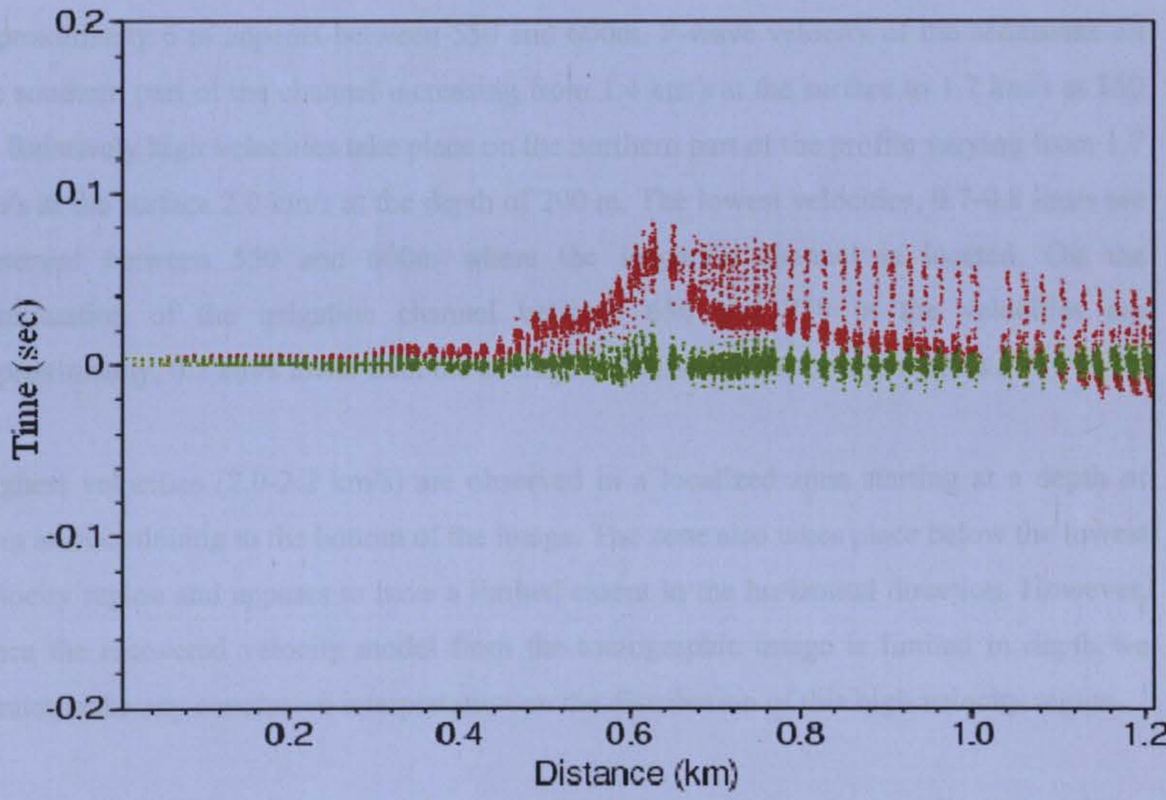

Figure 6.8. Travel time residuals for preferred starting (red) and final model (green).

Figures 6.9 - 6.11 display the results of the tomographic inversion and ray coverage for the final P-wave velocity model with three initial velocity models. Dependency on the initial models is not significant when the ray hitcount is large therefore the velocities are well resolved. A robust and high resolution travel time image requires dense ray sampling and rays crossing at variety of angles. Therefore, ray coverage is the main defining parameter for the resolution. The velocities at shallow depths above 20 m are not well constrained due to the lack of near offset data, as a result these velocities are sensitive to the initial model. The ray coverage indicates that the final velocity model is well constrained up to 170 m depth. Similar results were obtained from alternate initial models and different inversion parameters except at shallow depths, and where ray coverage is poor.

There is no available data on the thickness and the geometry of the basin. However, it is expected that the maximum thickness of the sediments is greater than 1.0 km. As a result, we do not expect to see the basement from the travel time tomography. The seismic profile crosses the fault between 600-700 meters. The irrigation channel with a width of approximately 6 m appears between 550 and 600m. P-wave velocity of the sediments on the southern part of the channel increasing from 1.4 km/s at the surface to 1.7 km/s at 150 m. Relatively high velocities take place on the northern part of the profile varying from 1.7 km/s at the surface 2.0 km/s at the depth of 200 m. The lowest velocities, 0.7-0.8 km/s are observed between 550 and 600m where the irrigation channel is located. On the continuation of the irrigation channel between 650 and 750 m the velocities are approximately, 0.2 km/s lower than the average velocities on the northern block.

Highest velocities (2.0-2.2 km/s) are observed in a localized zone starting at a depth of 80m and continuing to the bottom of the image. The zone also takes place below the lowest velocity region and appears to have a limited extent in the horizontal direction. However, since the recovered velocity model from the tomographic image is limited in depth we cannot make any conclusive interpretation on the distribution of this high velocity region.

Figures 6.12 - 6.14 show the final tomographic image and fan shots at distances of 0m, 200m and 400m, respectively. The high amplitude surface waves are observed at receivers near the fault zone. Since the amplitudes of the surface waves are decreasing fast for receivers away form the fault zone the observed wavefield indicate trapped waves generated along the fault zone. The separation of the surface waves and trapped waves from the body waves are apparent for the shots at greater distances (compare 0m and 600m fan shots). It is also important to realize that there is significant asymmetry of the wavefield on both sides of the fault zone. The arrival times on the northern part of the fault zone show interesting character. There is a large travel time jump at a distance of 900m. We cannot directly correlate such a travel time jump by the final tomographic image. If the high velocity anomaly is not local but has larger spatial dimensions or has continuity along the fault zone, it may create asymmetries on the wavefield. Such asymmetries are created, e.g., by head waves propagating along vertical discontinuities with higher velocities.

Figure 6.15 shows the final tomographic image and two shot gathers from each side of the fault zone. If there is a high velocity body present in the medium this will create travel time anomalies on the first arrivals as well as diffraction pattern on the wavefield. The first shot gather presented in the figure has a clear diffraction pattern with the apex at the distance of approximately 500 m. This is an independent confirmation of the high velocity anomaly observed on the tomographic image. The second shot gather displayed on the Figure 6.15, on the other hand, contains fault zone trapped waves between distances of 650 and 750 m. Fault zone trapped wave are clearly separated from surface waves with large amplitudes.

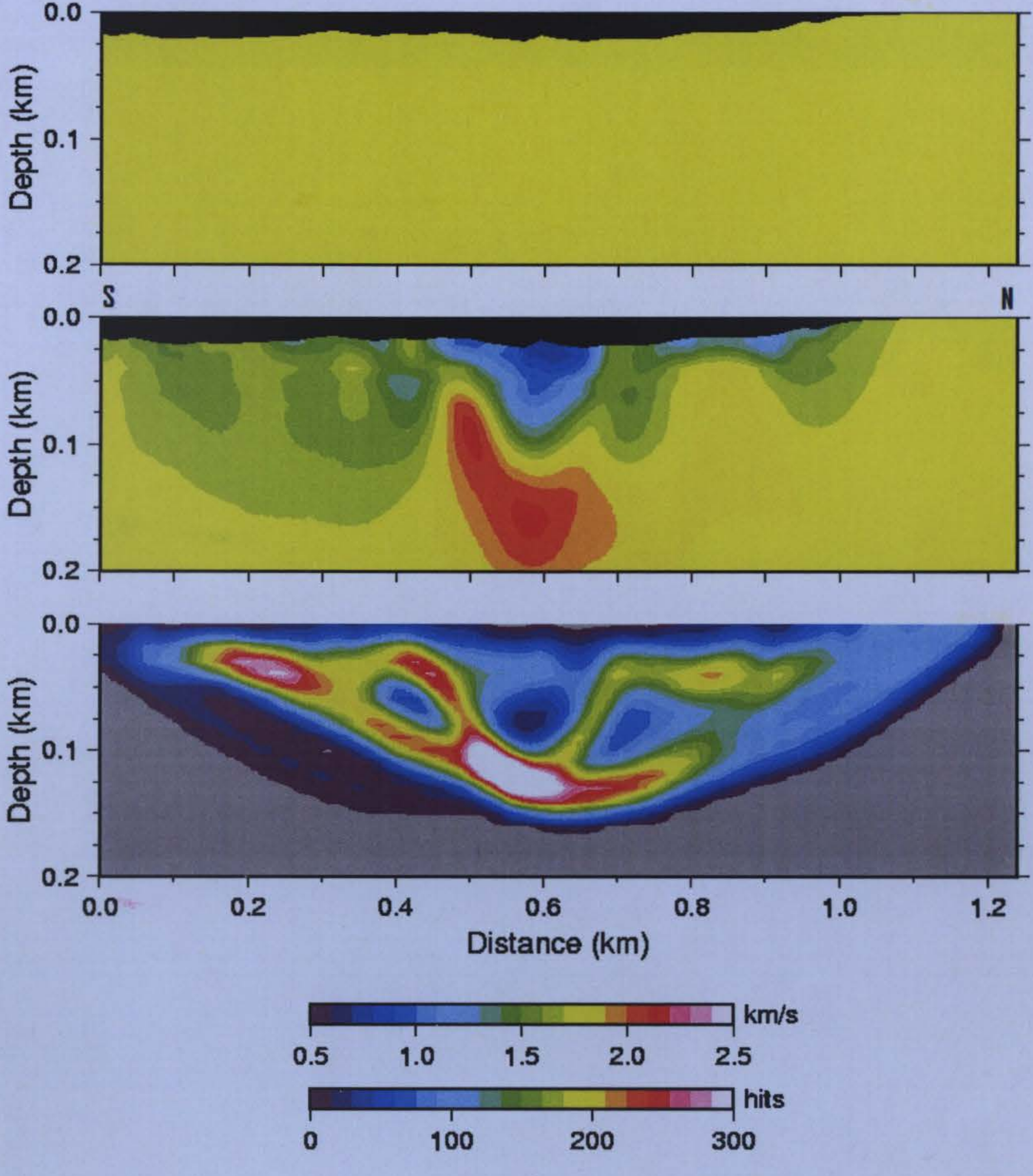

Figure 6.9. Final model from regularized inversion for the constant velocity model. Upper figure is the initial velocity model, middle shows the final P-wave velocity model and lower figure is the ray hitcount.

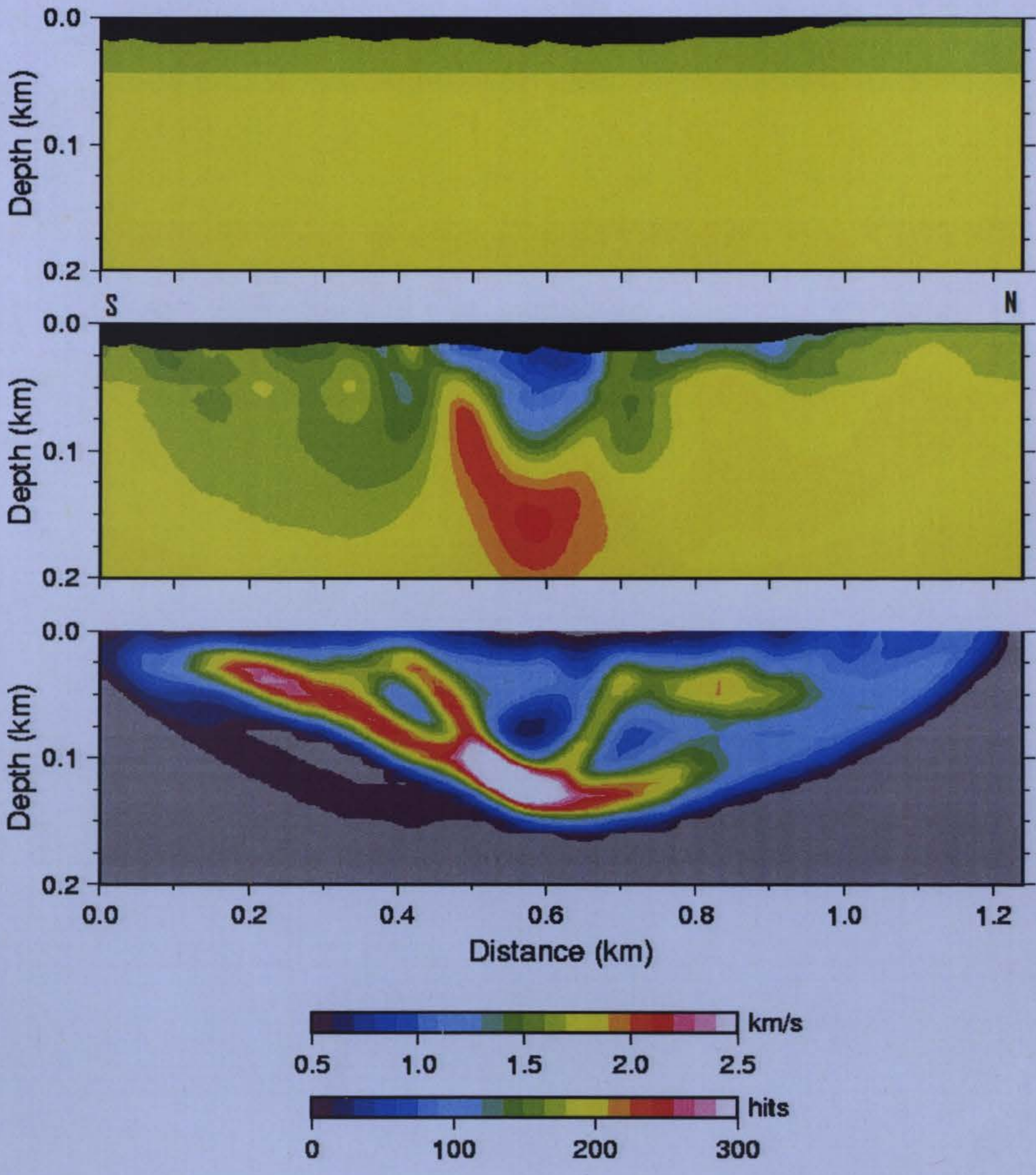

Figure 6.10. Final model from regularized inversion for the three-layer velocity model. Upper figure is the initial velocity model, middle shows the final P-wave velocity model and lower figure is the ray hitcount.

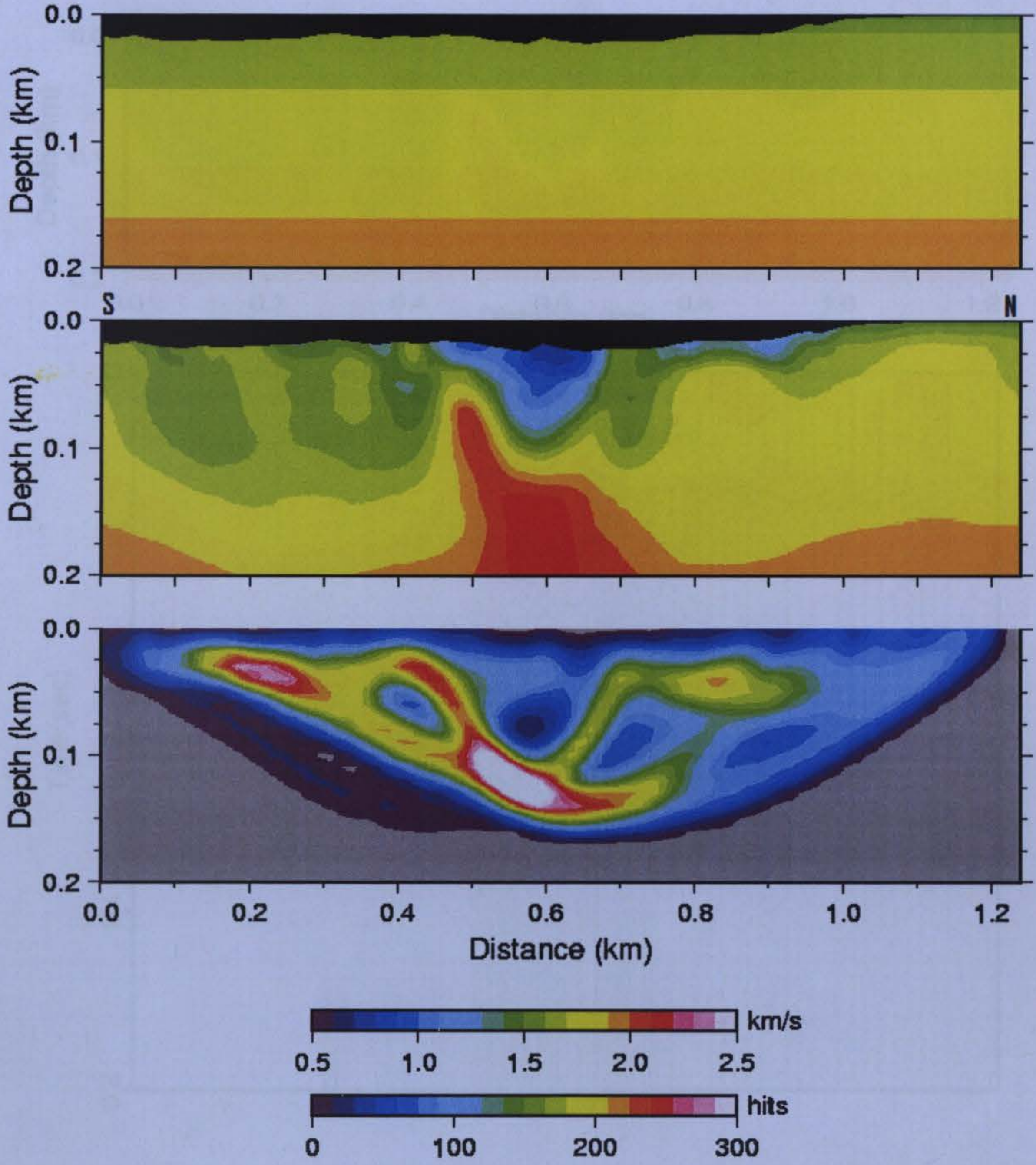

Figure 6.11. Final model from regularized inversion for the gradient velocity model. Upper figure is the initial velocity model, middle shows the final P-wave velocity model and lower figure is the ray hitcount.

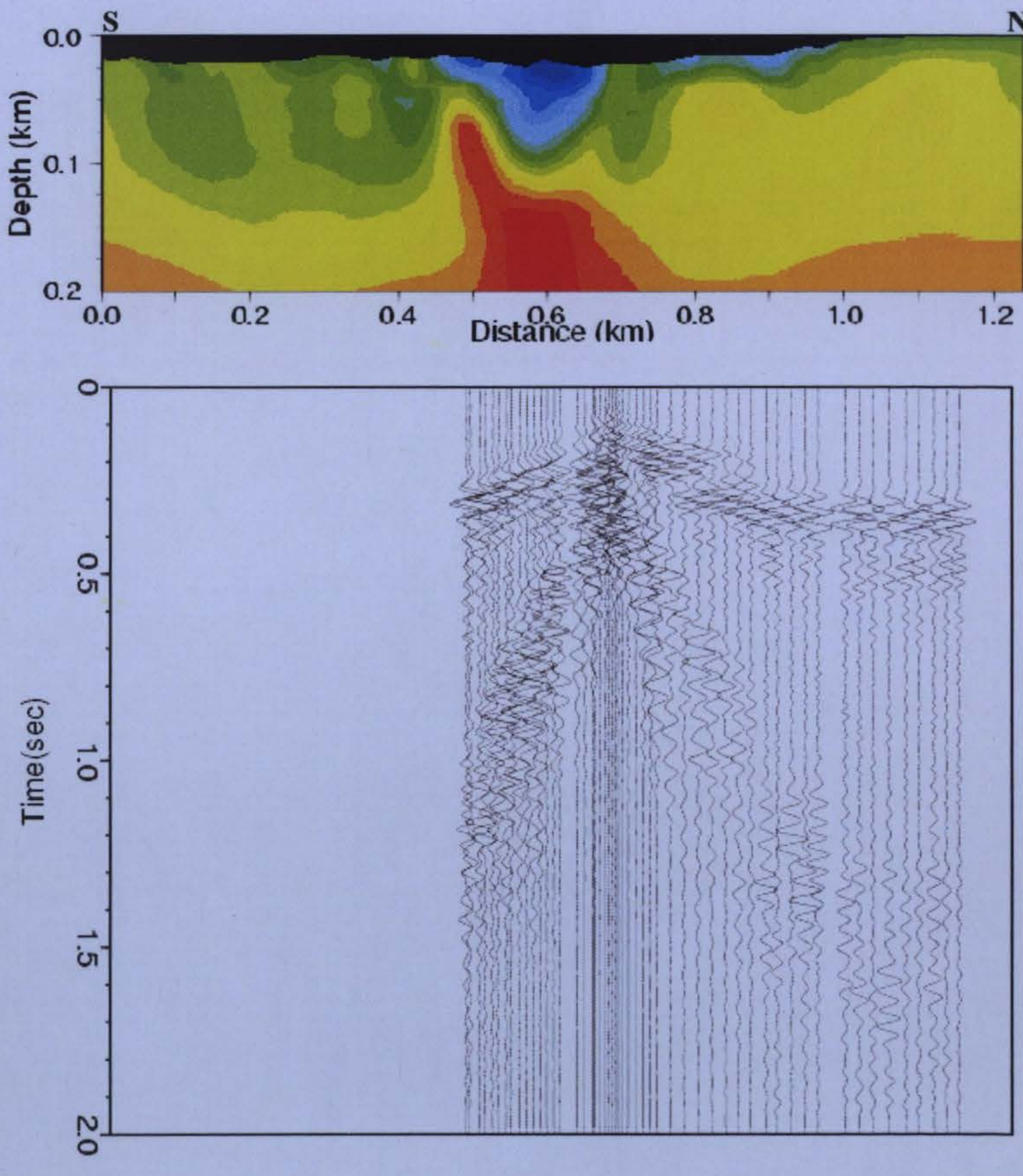

Figure 6.12. The final tomographic image and fan shot at the distance of 0m.

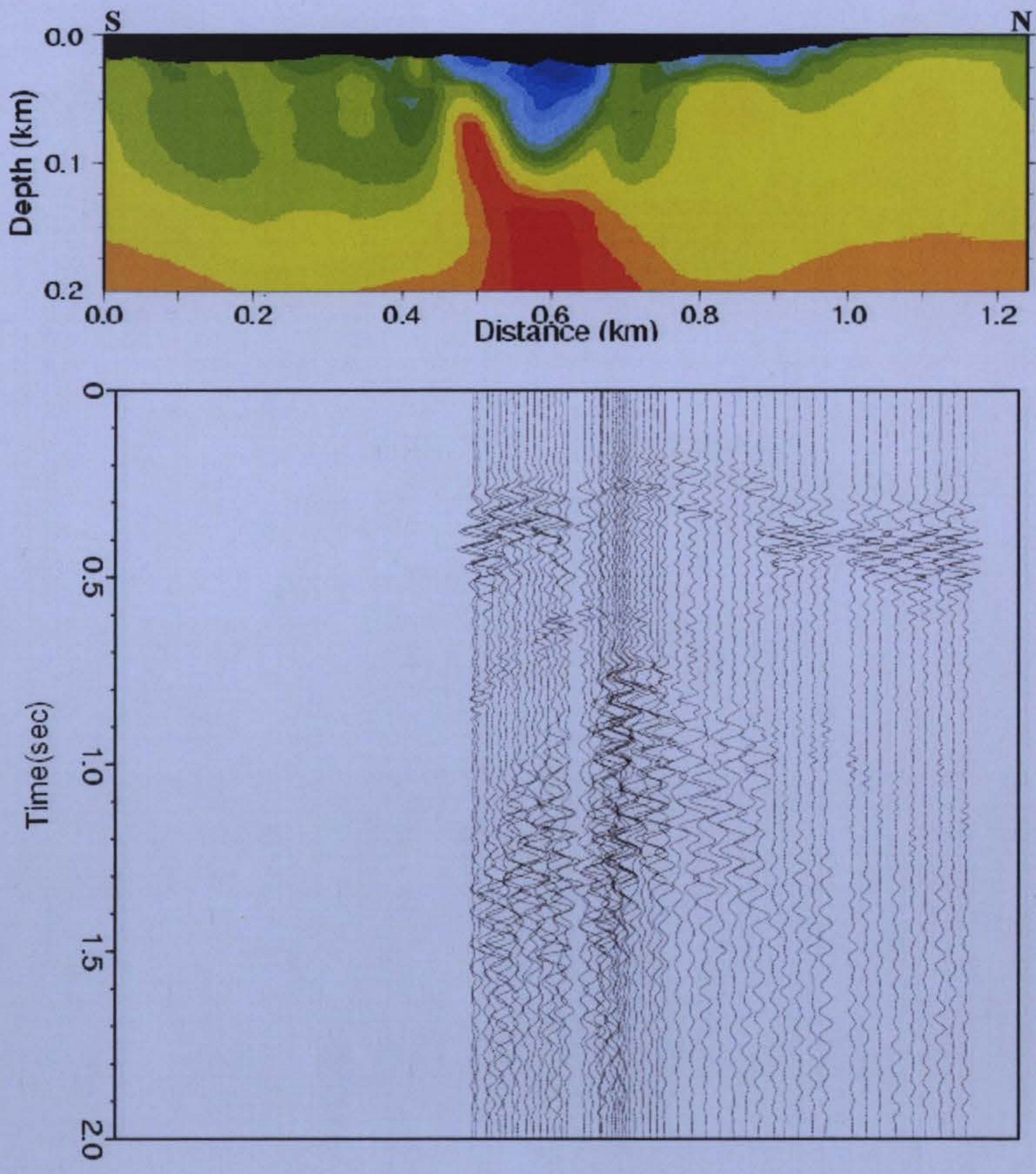

Figure 6.13. The final tomographic image and fan shot at the distance of 200m.

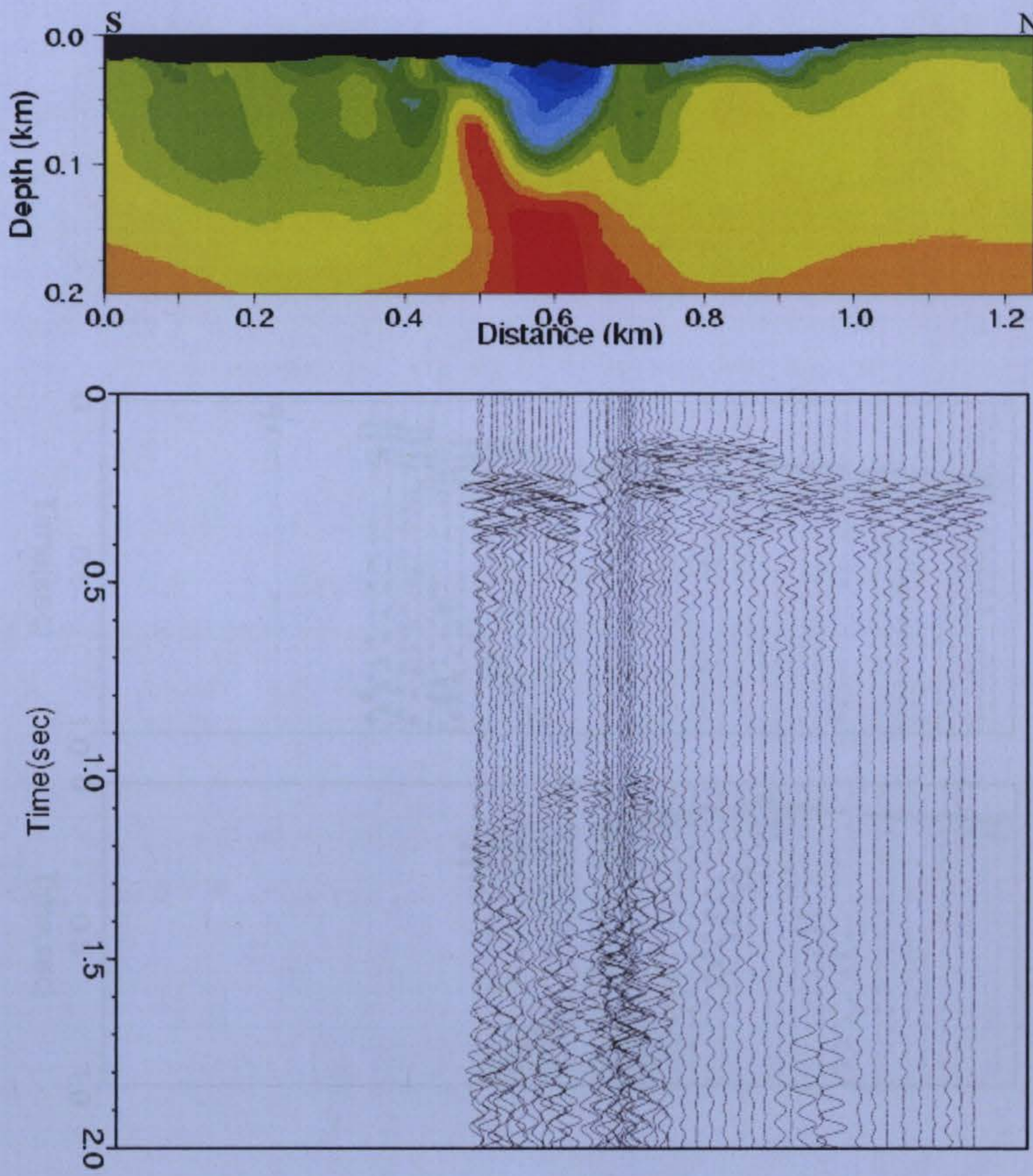

Figure 6.14. The final tomographic image and fan shot at the distance of 400m.

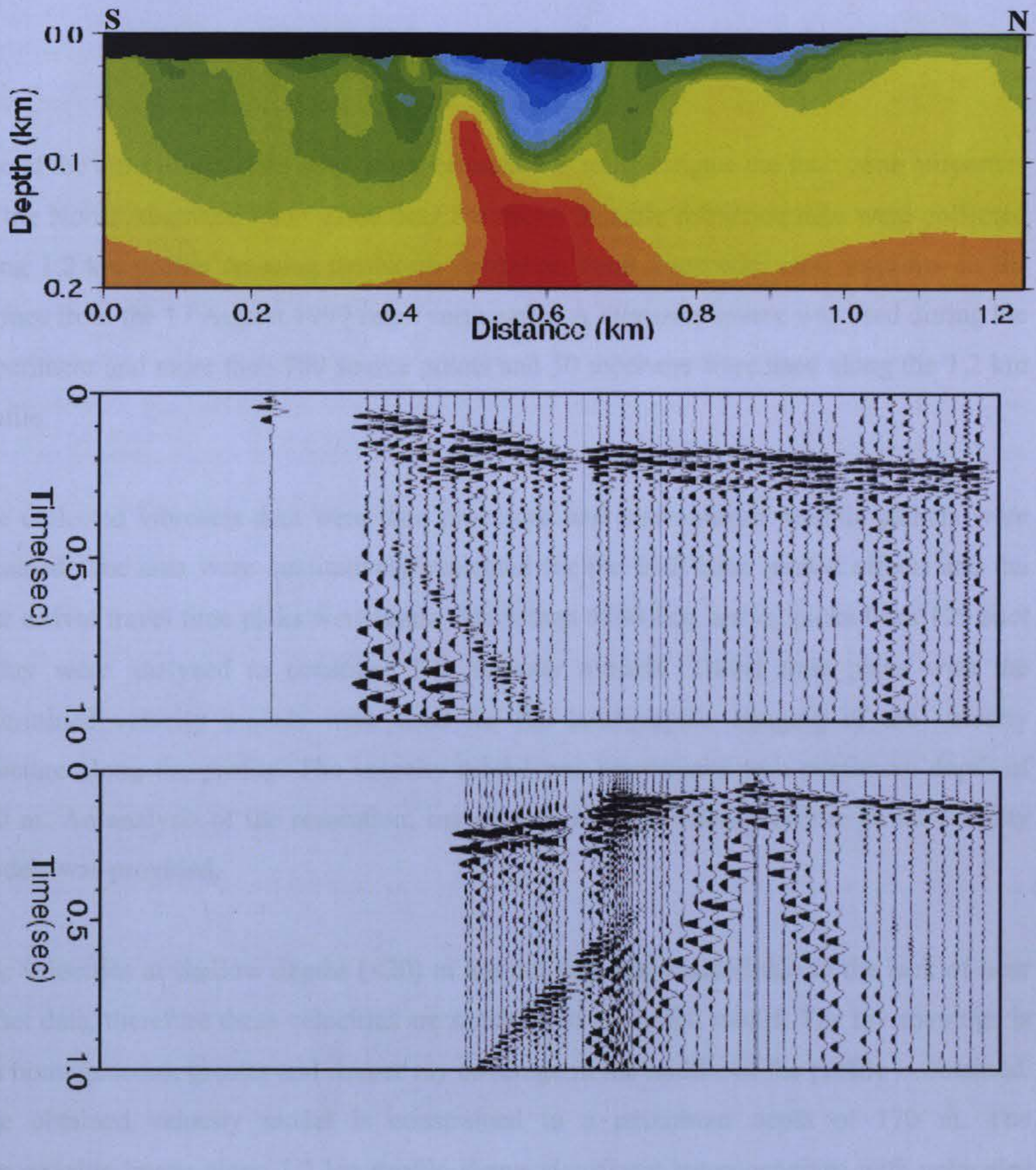

Figure 6.15. The final tomographic image and two shot gathers, which are plotted with a reducing velocity of 2 km/s, along the profiles.

7. DISCUSSION AND CONCLUSIONS

One of the aims of the 2003 seismic experiment was to investigate the fault zone properties on the North Anatolian Fault Zone near Sarımeşe. Seismic refraction data were collected along 1.2 km profile crossing the North Anatolian Fault Zone with clear imprints on the surface from the 17 August 1999 İzmit earthquake. A vibroseis source was used during the experiment and more than 180 source points and 50 receivers were used along the 1.2 km profile.

The collected vibroseis data were then processed and conventional seismic gathers were obtained. The data were qualitatively evaluated for the fault zone related effects and the first arrival travel time picks were made. More than 6500 first arrival picks from 129 shot gather were analyzed to construct 1-D velocity models. Travel time picks with the determined velocity models were used for the tomographic imaging of the velocity structure along the profile. The velocity model was constrained to a maximum depth of 200 m. An analysis of the resolution, smoothness and dependency on the initial velocity models was provided.

The velocities at shallow depths (<20) m are not well constrained due to the lack of near offset data, therefore these velocities are sensitive to the initial model. The ray coverage is not homogeneous, greater and deeper ray coverage in the middle of the profile is obtained. The obtained velocity model is constrained to a maximum depth of 170 m. The tomographic image along 1.2 km profile shows significant heterogeneities with velocities varying from 0.7 km/s to 2.2 km/s.

The fault was clearly exposed on the surface and the thickness of the sediments in the basin is expected to be several hundred meters. The northern part of İzmit Gulf is essentially consists of young shallow sediments, beneath these lie a Triassic and Paleozoic sandstone, clay stone and marn where relatively high velocities take place. P-wave velocities vary from 1.7-2.0 km/s down to 200 m depth. The velocities of the sediments, on the southern part that corresponds to an olistolitic complex, which is composed of Eosen volcanics (schist, serpentine and andesit), differ from 1.4 to 1.7 km/s and decreases to 1.4 km/s within the fault zone down to 100-150 m depth.

Another low velocity zone of 0.9km/s observed right next to 1999 İzmit earthquake fault zone and explained as an effect of irrigation channel when the geometry of the experiment is considered. A localized body of high velocity (2.2 km/s) with respect to the surrounding units, between 500-700 meters, observed in this region is thought to be related to a buried andesitic ridge. However, since the recovered velocity model from the tomographic image is limited in depth we cannot make any conclusive interpretation on the distribution of this high velocity body. After analyzing the fan shots, we realized that there is significant asymmetry of the wavefield on both sides of the fault zone. There is a large travel time jump at between distances of 800 and 900m. Such a travel time jump cannot be correlated by the final tomographic image. If the high velocity anomaly is not local but has larger spatial dimensions or has continuity along the fault zone it may create asymmetries on the wavefield and would create travel time anomalies on the first arrivals as well as diffraction pattern on the wavefield. The clear diffraction patterns, observed in the shot gathers, are an independent confirmation of the high velocity anomaly observed on the tomographic image. The tomographic results clearly indicate that the fault zone is approximately 100m wide and this information is correlated with the seismic studies performed in the same region.

Seismic observations near the fault zone show motion amplifications, long period oscillations, head waves, and travel time anomalies. These anomalies can be used to determine internal structure of fault zone layer. Further studies such as waveform modeling and detailed analysis of trapping structure can be useful to define the fault zone parameters.

8. REFERENCES

Aki, K., 1982. Three-dimensional inhomogeneities in the lithosphere and asthenosphere: evidence for decoupling in the lithosphere and flow in the asthenosphere., Rev. Geophys. Space Phys., 20, 161-170.

Aki, K., and Lee, W. H. K., 1976. Determination of three-dimensional velocity anomalies under a seismic array using first P- arrival time from local earthquakes, 1. A homogeneous initial model, J. Geophys. Res., 81, 4381-4399.

Aki, K., Christofferson, A. and Husebye, E.S., 1976. Three-dimensional seismic structure of the lithosphere under Montana LASA, Bull. Seismol. Soc. Am., 66, 501-524.

Aki, K., Christofferson, A. and Husebye, E. S., 1977. Determination of the three dimensional seismic structure of lithosphere, J.Geophys. Res., 82, 277-296.

Aktar, M., Özalaybey, S., Karabulut, H., P. Bouin, M., Tapirdamaz, C., Biçmen, F., Yörük, A., Bouchon, M., 2004. Spatial variation of.aftershock activity across the rupture zone of the 17 August 1999 Izmit Earthquake, Turkey, Tectonophysics, 391, 325-334.

Ambrasseys, N., 2002. The seismic activity of the Marmara Sea Region over the last 200 years, Bull. Seismol. Soc. Am., 92, 1-18.

Ambrasseys, N., and Jackson, J.A., 2000. Seismicity of the Sea of Marmara (Turkey) since 1500, Geophys. J. Int., 141, F1-F6.

Arpat, E. and Şaroğlu F., 1972. Doğu Anadolu Fayı ile ilgili bazı gözlem ve düşünceler. MTA Dergisi 73, 1-9.

Barka, A., and Kadinsky-Cade, K., 1988. Strike-slip fault geometry in Turkey and its influence on earthquake activity, Tectonics, 7, 663– 684.

Barka, A., 1992. The North Anatolian Fault Zone, Annales Tectonicae, T, 164-195.

Barka, A. and Gülen, L., 1988, New Constraints on age and total offset of the North Anatolion fault zone: implications for tectonics of the Eastern Medditeranean region. In "1987 Melih Tokay Symp." Spec. Publ. METU. Ankara, Turkey, 39-65.

Bauer, K., Schulze, A., Ryberg, T., Sobolev, S. V., Weber, M. H., 2003. Classification of lithology from seismic tomography: A case study from the Messum igneous complex, Namibia, J. Geophys. Res.,108(B3),2152, doi:10.1029/2001JB001073, 2003.

Ben Zion, Y., Peng, Z., Okaya, D., Seeber, L., Armbruster, J.G., Özer, N.,Micheal, A. J., Barış, Ş., and Aktar, M. 2003. A Shallow Fault Zone Structure Illuminated by Trapped Waves in the Karadere-Dzce Branch of the North Anatolian Fault, Western Turkey, Geophys. J. Int. 152, 699–717.

Ben-Zion, Y. and Sammis, C.G., 2003. Characterization of Fault Zones, Pure Appl. Geophys., 160, 677-715.

Bouchon, M., and Karabulut, H., 2002. A note on seismic activity near the eastern termination of the İzmit rupture in the hours preceding the Düzce earthquake, Bull. Seism. Soc. Am. 92, no. 1, 406–410.

Bülent Tank, Honkura,Y., Ogawa, Y., Matsushima, M., 2005. Magnetotelluric imaging of the fault rapture area of the 1999 Izmit (Turkey) earthquake, Physics of the Earth and Planetary Interiors, 150, 213-225.

Clayton, R.W. and Comer, R.P., 1983. A tomographic analysis of mantle heterogeneities from body wave travel time (abstract), Eos, Trans. Am. Geophys. Union, 64, 776.

Day, J., Peirce, C., Sinha, M., 2001. Three-dimensional crustal sturucture and magma chamber geometry at the intermediate-spreading, back-arc Valu Fa Ridge, Lau Basin results of a wide-angle seismic tomographic inversion, Geophys J.Int., 146, 31-52.

Dewey, J.F. and Şengör, A.M.C., 1979. Aegean and surroundings regions: Complex multiplate and continuum tectonics in a convergent zone, Geolog. Soc. of Amer. Bull., 90, 84–92.

Dziewonski, A.M. and Anderson, D.L., 1984. Seismic tomography of Earth's interior, Am. Sci., 721, 483-394.

Dziewonski, A.M., 1984. Mapping the lower mantle: determination of lateral heterogeneity in P velocity up to degree and order 6. J.Geophys.Res., 89, 5929-5952.

Eberhart-Phillips, D., 1986. Three-dimensional velocity structure in northern California Coast Ranges for inversion of local earthquakes arrival times, Bull. Seismol. Soc. Am., 76, 1025-1052.

Eberhart-Phillips, D., 1989. Investigations of crustal structure and active tectonic processes in the coast ranges, central California., Ph.D. Thesis, Stanford University, Stanford.

Eberhart-Phillips, D., Stanley, W.D., Rodriquez, B.D. and Lutter, W.J., 1995. Surface seismic and electrical methods to detect fluids related to faulting, J. geophys. Res., 97, 12 919–12 936.

Grevemeyer, I., Flueh, E., Reichert, C., Bialas, J., Klaschen, D., Kopp, C., 2001. Crustal architecture and deep structure of the Ninetyeast Ridge hotspot trail from active-source ocean bottom seiemology, Geophys J.Int., 144, 414-431.

Haslinger, F. and Kissling, E., 2001. Investigating effects of 3-D ray tracing methods in local earthquake tomography, Phys.Earth planet.Inter.,123, 103-114.

Hirahara, K., 1977. A large-scale three-dimensional seismic structure under the Japan Islands and the Sea of Japan, J. Phys. Earth, 25, 393-417.

Hole, J.A. and Zelt, B.C., 1995. Three-dimensional finite-difference reflection travel times, Geophys. J. Int., 121, 427-434.

Hole, J.A., Zelt, C.A. and Pratt, R.G., 2005. Advances in controlled-source seismic imaging. Eos Trans. Amer. Geophys. Union, 86, 177 & 181

Honkura, Y., Işıkara, A.M., Oshiman, N., İto, A., Uçer, B., Baris, S., Tuncer, M.K., Matsushima, M., Pektas, R., Çelik, C., Tank, B., S., Takahashi, F., Nakanishi, M., Yoshimura, R., Ikeda, Y., Komut, T., 2000. Preliminary results of multidisciplinary observations before, during and after the Kocaeli (İzmit) earthquake in the western part of North Anatolian Fault Zone, Earth Planets Space, 52, 293-298.

Hoşgören, M.Y., 1997. Geomorphology of basin of the Gulf of İzmit. İzmit Körfez'inin Kuvaterner stifi, Gölcük 343-348.

Jackson, D. D., 1972. Interpretation of inaccurate, insufficient, and inconsistent data: Geophysical Journal of the Royal Astronomical Society, 28, 97-109.

Karabulut, H., Özalaybey, S., Taymaz, T., Aktar, M., Selvi, O., Kocaoğlu, A., 2003. A Tomographic Image of the shallow crustal structure in the Eastern Marmara, Geophysical Research Letters, 30, 24-2277.

Karabulut, H., Bouin, M., Bouchon, M., Dietrich, M., Cornou, C. and Aktar, M., 2002. The seismicity in the Eastern Marmara Sea after the 17 August 1999 İzmit Earthquake, Bull. Seism. Soc. Am, 92, 382-393.

Ketin, İ., 1973. Umumi Jeoloji (General Geology), Published by İTÜ, 4th Ed.

Kissling, E., Ellswoth, W.L., Eberhart-Philips, D., Kradolfer, U., 1994. Initial reference models in seismic tomography. J. Geophys. Res. 99, 19635-19646.

Koçyiğit, A. and Yiğitbaş, E., 2002. A Section Through Precambrian Basement and Surface Ruptures of 1999 Earthquakes, A Post Symposıum Excursion FT-1 Guide Book, 2002

Lawson, C.L. and Hanson, R.J., 1974. Solving Least Squares Problems, Prentice- Hall, Englewood Cliffs. NJ.

Levin, K.F. and Lines, R.L., 2002. Inversion of Geophysical Data, Geophysics reprint series No.9.

Lines, L.R. and Treitel, S., 1984. A Review of Least Square Inversion and its Application to Geophysical Problems, Geophysical Prospecting 32, 159-186.

McKenzie, D., 1972. Active tectonics of the Mediterranean region, Geophys. J. R. Astr. Soc., 30(2), 109– 185.

Menke, W., 1989. Geophysical Data Analysis: Discrete Inverse Theory, Academic Press, Inc., San Diego.

Nakamura, 2002. P-wave velocity structure of the crust and its relationship to the occurence of the 1999 Izmıt, Turkey earthquake and aftershocks, Bull. Seism. Soc. Am, 92, 330-338.

Nolet, G., 1985. Solving or resolving inadequate and noisy tomographic systems, J. Comput. Phys., 61, 463-482.

Okay, A.I., 1986. Tectonics Units and sutures in the pontides, Northern Turkey.Tectonic evolution of the Tethyan Region, Nato ASI Series. Series C-Vol.259, 109-116.

Oral, M.B., Reilinger, R.E., Toksöz, M.N., Barka, A. and Kınık, İ. 1993. Preliminary Results of 1988 and 1990 GPS Measurement in Western Turkey and their Tectonic implications, Geodynamics, 23, 407-416.

Özalaybey, S., Ergin, M., Aktar, M., Tapırdamaz, C., Biçmen, F. and Yörük, A., 2002. The 1999 İzmit Earthquake Sequence in Turkey: Seismological and Tectonic Aspects, Bull. Seism. Soc. Am, 92, 376-386.

Peng, Z. and Ben-Zion, Y., 2005. Temporal changes of shallow seismic velocity around the Karadere-Duzce branch of the north Anatolian fault and strong ground motion, Pure Appl. Geophys.

Pereyra, V., Lee, W.H.K. and Keller, H.B., 1980. Solving two-point seismic raytracing problems in heterogeneous medium, Pt. 1. A general adaptive finite difference method, Bull. Seismol. Soc. Am., 70, 79-99. NY.

Phillips, D.E., Stanley, W.D., Rodrıquez, B.D., Lutter, W.J. 1995. Surface seismıc and electrical methods to detect fluids related to faulting, Journal Of Geophysics Resarch, Vol,100, 12919-12936.

Phillips, W.S. and Fehler, M.C., 1991. Traveltime tomography: a comparison of popular methods, Geophysics, 56, 1639-1649.

Şengör, A.M.C, Görür, N. and Şaroğlu F., 1985. Strike-slip faulting and related basin formation in zones of tectonic escape : Turkey as a case study, in Strike-slip deformation, basin formation and sedimentation, edited by K.T. Biddle and N.C Blick, pp. 227-264, Soc. Econ. Palen. Mine. Spec. Publication.

Şengör, A.M.C. and Yılmaz, Y., 1981. Tethyan evolution of Turkey: a plate tectonic approach. Tectonophysics 75, 181-241.

Shaw, P.R., and Orcutt, J.A., 1985. Waveform inversion of seismic refraction data and applications to young Pacific crust: Geophys. J. Roy. Astr. Soc., 82, 375-414.

Stein, S. and Wysession, M., 2003. An Introduction to Seismology, Earthquakes And Earth Structure, Blackwell Publishing, Cornwall.

Tarantola, A., and Valette, B., 1982. Generalized non-linear inverse problems solved using the least squares criterion: Rev. of Geophys. and Space Phys., 20, 219-232.

Thurber, C.H., 1993. Local earthquake Tomography: velocities and Vp/Vs theory. In: Iyer, H.M., Hirahara, K. (Eds.), Seismic Tomography: Theory and Practice. Chapman and Hall, London, pp. 563-583.

Thurber, U.C.H, 1987. A fast algorithm for two-point seismic ray tracing. Bull. Seismol. Soc. Am. 77, 972-986.

Vidale, J.E., 1990. Finite-difference calculation of travel times, Bull. Seism. Soc. Am., 78, 2062-2076.

Wesson, R.L., 1971. Travel-time inversion for laterally inhomogeous crustal velocity models, Bull. Seismol. Soc. Am., 61, 729-746.

Woodhouse, J.H. and Dziewonski, A.M., 1984. Mapping the upper mantle: Three dimensional modelling of earth structure by inversion of seismic waveforms, J. Geophys. Res., 89, 5953-5986.

Yılmaz, Y., 1990. Comparison of young volcanic associations of western and eastern Anatolia formed under a compressional regime: A review, J. Volcanol. Geotherm. Res., 44, 69– 87.

Yılmaz, Y., Tüysüz, O., Yiğitbaş, E., Genç, Ş.C., Şengör, A.M.C., 1997. Geology and Tectonic Evolutıon of the Pontides, AAPG Memoir 68, 183-226.

Yılmaz, Y., Genç, Ş.C., Yiğitbaş, E., Bozcu, M., Yılmaz, K., 1995. Geologıcal evolutıon of the late Mesozoic continental margin of Northwestern Anatolia, Tectonophysics 243(1995),155-171

Zelt, C., Smith, R.B., 1992. Seismic traveltime inversion for 2-D crustal velocity sturucture, Geophys J.Int., 108, 16-34.

Zelt, C.A. and Barton, P.J., 1998. Three-dimensional seismic refraction tomography: a comparision of two methods applied to data from Faeroe Basin, J. Geophys. Res., 103, 7187-7201.

Zhao, D., 1990. A tomographic study of seismic velocity structure in the Japan Islands, PhD Thesis, Tohoku University.

Zhao, W., Mechie, J., D. Brown, L., Guo, J., Haines, S., Hearn, T., L. Klemperer, S., S. Ma, Y., Meissner, R., D. Nelson, K., F. Ni, J., Pananont, P., Rapine, R., Ross, A., Soul, J., 2001. Crustal sturucture of central Tibet as derived from project INDEPTH wide-angle seismic data, Geophys J.Int., 145, 486-498.